

PAPER



Cite this: *Dalton Trans.*, 2020, **49**, 8933

An unprecedented polyhydroxycarboxylic acid ligand bridged multi-Eu^{III} incorporated tellurotungstate and its luminescence properties†

Yan Zhang,^a Dan Wang,^a Baoxing Zeng,^a Lijuan Chen,^{*a} Junwei Zhao ^{*a} and Guo-Yu Yang ^{*b}

The first polyhydroxycarboxylic acid ligand bridged multi-Eu^{III}-incorporated tellurotungstate $K_{14}H_{10}[Eu_4(H_2O)_4W_6(H_2glu)_4O_{12}(B-\alpha-TeW_9O_{33})_4] \cdot 60H_2O$ ($H_6glu = D$ -gluconic acid) (**1**) was synthesized via an organic ligand-driven self-assembly strategy. The polyhydroxycarboxylic acid ligand bridged tetrameric polyoxoanion $[Eu_4(H_2O)_4W_6(H_2glu)_4O_{12}(B-\alpha-TeW_9O_{33})_4]^{24-}$ in **1** can be viewed as an aggregation of four trivacant Keggin $[B-\alpha-TeW_9O_{33}]^{8-}$ fragments and an innovative heterometallic $[Eu_4(H_2O)_4W_6(H_2glu)_4O_{12}]^{8+}$ cluster, in which four high-coordinate polyhydroxy flexible H_2glu^{4-} ligands chelate W and Eu centers through carboxyl and hydroxyl groups, giving rise to a heterometallic cluster. The hexagonal packing of the tetrameric polyoxoanions in **1** along the *c* axis provides excellent porous channels, which greatly increases the specific surface area of the whole framework and may be of benefit for fluorescence sensing in aqueous solution. **1** can function as a “turn-off” luminescence sensor to detect Cu^{2+} ions in aqueous solution. The limit of detection (LOD) of the **1**-sensor is 8.82×10^{-6} mM, which is the lowest among the reported polyoxometalate-based fluorescence sensors. As for the Cu^{2+} -quenching system, it can function as an “off-on” sensor to detect cysteine in an aqueous system, affording a LOD of 1.75×10^{-4} mM. This work opens up an avenue to broaden the applications of polyoxometalate-based materials in the optical intelligence detection field.

Received 26th February 2020,
Accepted 3rd June 2020

DOI: 10.1039/d0dt00729c

rsc.li/dalton

Introduction

Smart materials can respond to environmental changes around them in a predictable and useful manner, which has led to their fascinating use in diverse fields such as thermology, mechanics, electronics and optics, *etc.*¹ Designing and developing novel smart optical response materials to continuously perceive different exteroceptive stimuli is a cutting-edge research hotspot in the fluorescence (FL) sensing field.² To this end, rare-earth (RE)-based materials are often used to manufacture FL chemosensors because RE ions with rich electron energy levels show outstanding luminous properties under light excitation. For this reason, recently there has been

a mushrooming in research enthusiasm in fabricating such materials.³

Polyoxometalates (POMs), as unique inorganic early transition-metal metal-oxo anionic clusters, provide multitudinous oxo-active sites to capture RE ions, giving rise to RE-functionalized POM materials that have various applications in optics, magnetism, medicine and catalysis.⁴ Besides this, the oxygen-to-metal charge transfer ($O \rightarrow M$ LMCT) of POMs could further sensitize the FL properties of RE ions.⁵ RE-containing tungstotellurates (RECTTs), as a significant branch of materials science, possess good water solubility, which provides an excellent possibility for RECTTs to detect trace substances in aqueous solution.⁶ Currently, some RECTTs with remarkable structures have been resoundingly isolated, but the great progress in this field is the synthesis of purely inorganic architectures.⁶ The design, synthesis and discovery of unique inorganic-organic RECTT hybrids are still in their infancy. It should be noted that organic groups are rich binding sites for oxyphilic RE ions, thus, introducing multi-functional organic groups to the RECTT system can offer the great possibility of constructing unexpected organic-inorganic hybrid poly(RECTT) aggregates. For example, in 2017, we for the first time reported a family of 2-picolinic-acid

^aHenan Key Laboratory of Polyoxometalate Chemistry, College of Chemistry and Chemical Engineering, Henan University, Kaifeng, Henan 475004, China. E-mail: ljchen@henu.edu.cn, zhaojunwei@henu.edu.cn

^bMOE Key Laboratory of Cluster Science, School of Chemistry, Beijing Institute of Technology, Beijing 100081, China. E-mail: ygy@bit.edu.cn

†Electronic supplementary information (ESI) available: Related structural figures; IR, luminescence and ESI-MS spectra and TG curve of **1**. CCDC 1936173. For ESI and crystallographic data in CIF or other electronic format see DOI: 10.1039/d0dt00729c

decorated tetrameric RECTTs $[\text{RE}_2(\text{H}_2\text{O})_4(\text{pica})_2\text{W}_2\text{O}_5][(\text{RE}(\text{H}_2\text{O})\text{W}_2(\text{Hpica})_2\text{O}_4)(\text{B}-\beta\text{-TeW}_8\text{O}_{30}\text{H}_2)]^{24-}$ ($\text{RE} = \text{La}^{3+}, \text{Ce}^{3+}, \text{Nd}^{3+}, \text{Sm}^{3+}, \text{Eu}^{3+}, \text{Hpic} = 2\text{-picolinic acid}$).⁷ In the same year, we addressed a class of newfangled organotin–RE incorporated tungstotellurates (TTs) $\{[\text{Sn}(\text{CH}_3)\text{W}_2\text{O}_4(\text{IN})][(\text{B}-\alpha\text{-TeW}_8\text{O}_{31})\text{RE}(\text{H}_2\text{O})(\text{Ac})]_2\}^{20-}$ ($\text{RE} = \text{Ce}^{3+}, \text{Pr}^{3+}, \text{Nd}^{3+}, \text{Sm}^{3+}, \text{Eu}^{3+}, \text{Gd}^{3+}, \text{Tb}^{3+}$, HIN = isonicotinic acid, HAc = acetic acid) simultaneously containing three types of organic ligands.⁸ Recently, the first 2,5-pyridinedicarboxylic acid connected 3d–4f heterometal encapsulated tetrameric TTs $[\text{RE}_2(\text{Ac})_2(\text{H}_2\text{O})_4\text{Fe}_2(\text{Hpdca})_2(\text{B}-\beta\text{-TeW}_9\text{O}_{33})_2][\text{RE}_2(\text{H}_2\text{O})_8\text{Fe}_2(\text{Hpdca})_2(\text{B}-\beta\text{-TeW}_9\text{O}_{33})_2]^{14-}$ ($\text{RE} = \text{Eu}^{3+}, \text{Tb}^{3+}, \text{Dy}^{3+}, \text{Er}^{3+}$, H₂pdca = 2,5-pyridinedicarboxylic acid) were discovered by Song's group.⁹ It can be apparently seen that investigations on neoteric polyhydroxycarboxylic acid flexible ligand containing poly(RECTT) aggregates are still unexplored, even though several inorganic–organic hybrid RECTTs with N-heterocyclic carboxylic acid ligands have been reported. With this research background in mind, we adopted the following synthetic tactics to construct novel polyhydroxycarboxylic acid flexible ligand containing poly(RECTT) aggregates: (a) the convenient and easy-to-use one-step self-assembly strategy on the basis of simple commercial initial reagents was chosen as a preparative method not only because no appropriate available TT precursor can be utilized as an initial reagent, but also because the effectiveness of the one-step self-assembly strategy has led to some unexpected gigantic poly(POM)s.¹⁰ (b) The stereochemically active TeO_3^{2-} anion with lone pair electrons as an effective template can induce tungstates to form open-pocket TT fragments,^{6a,11} which facilitates the incorporation of RE cations into the backbone of TT fragments in targeted products. Moreover, the stereochemically active TeO_3^{2-} anion can even serve as a linking group to integrate different TT fragments and RE cations together. (c) In this paper, the Eu^{3+} cation was used because of its strong FL emission and rich coordination modes,^{12,13} which gives us an excellent chance of creating charming Eu^{3+} -containing TTs as FL sensors. Besides this, the narrow line emission bands assigned to the 4f–4f transitions of the Eu^{3+} ion are beneficial for increasing the sensitivity of the sensor compared with the broad emission bands of organic molecules or quantum dots. (d) Water-soluble D-gluconic acid (H_6glu) with five hydroxy groups and one carboxyl group can connect different metal (RE and W) centers together and give rise to special multi-RE-W heterometallic connexons to build up polyhydroxycarboxylic acid flexible ligand containing poly(RECTT) aggregates.

As expected, an unprecedented tetrameric gluconic acid bridged multi- Eu^{3+} -incorporated TT aggregate $\text{K}_{14}\text{H}_{10}[\text{Eu}_4(\text{H}_2\text{O})_4\text{W}_6(\text{H}_2\text{glu})_4\text{O}_{12}(\text{B}-\alpha\text{-TeW}_9\text{O}_{33})_4]\cdot 60\text{H}_2\text{O}$ (**1**) was successfully obtained *via* an organic ligand-driven self-assembly strategy. Herein, the four flexible H_6glu ligands can be considered as cement to induce the aggregation of four trilacunary TT subunits and Eu^{3+} ions. Notably, such a five-coordinate mode for a polyhydroxycarboxylic acid ligand is very infrequent in the construction of POMs.¹⁴ Moreover, its benign FL properties and good water solubility make it the first new-fashioned RECTT-based FL “turn-off” sensor for detecting

Cu^{2+} ions in an aqueous system. The experimental results demonstrate that the FL sensor of **1** shows high FL activity and good selectivity for detecting the Cu^{2+} ion in aqueous solution, with a limit of detection (LOD) of 8.82×10^{-6} mM, making it the most sensitive POM-based FL sensor for detecting the Cu^{2+} ion in aqueous solution. The FL “turn-off” effect of **1** toward detecting the Cu^{2+} ion may be related to the fact the mechanism and contribution of the non-radiative relaxation in the presence of Cu^{2+} ions has been changed, which leads to the FL quenching of the **1**-sensor. With an increase in the concentration of the Cu^{2+} ion, the charge-transfer emission of **1** gradually weakens, causing a “turn-off” FL sensor to detect the concentration of the Cu^{2+} ion. In addition, we utilized the Cu^{2+} -quenching “turn-off” sensor as a “dark” background to further construct an “off-on” FL sensor to detect cysteine (Cys) in water, because studies have shown that the Cu^{2+} ion strongly chelates with Cys.¹⁵ The interference of the Cu^{2+} ion with the sensor is effectively reduced upon the addition of Cys. The FL intensity is also gradually recovered with the addition of Cys. In other words, an “off-on” FL sensor platform was successfully prepared for detecting Cys. Overall, this novel type of POM-based “turn-off” and “off-on” FL sensor would be a promising candidate with potential application to be applied in the detection fields, in environmental monitoring and clinical medical testing.

Experimental

Materials and characterization instruments

All the chemicals were of analytical grade and used without further purification. Infrared (IR) spectra were recorded on a Perkin–Elmer FT–IR spectrophotometer in the range of 4000–400 cm^{-1} using a powder sample pelletized with KBr. UV-vis spectra were recorded on a Mapada UV-6100 UV-vis spectrometer in the range of 190–400 nm in aqueous solution. Electrospray ionization mass spectrometry (ESI-MS) tests were performed on an AB SCIEX Triple TOF 4600 spectrometer operating in negative ion mode and the data was analyzed using the Peakview 2.0 software provided. The sample was prepared as described in the following and injected directly at a flow rate of 5 $\mu\text{L min}^{-1}$ using a syringe pump. **1** was prepared to a concentration of *ca.* 1.0 mg mL^{-1} . The solution was filtered and introduced to the spectrometer *via* direct injection. The ^{125}Te nuclear magnetic resonance (NMR) spectrum was acquired on a Bruker Avance NEO 600 spectrometer equipped with a broadband probe. The ^{125}Te NMR spectrum of **1** (42 mg mL^{-1}) in D_2O was measured at 158 MHz with a spectral width of 100 000 Hz, 3000 transients of 128 K data points and a recycle time of 1.5 to 2 s. The line broadening of the spectrum was 10 Hz and the reference was an external replacement sample of $\text{H}_2\text{TeO}_4\cdot 2\text{H}_2\text{O}$. C, H, O elemental analyses were carried out on a Perkin–Elmer 2400–II CHNS/O analyzer and K, Te, W and Eu elemental analysis was recorded on PerkinElmer Optima 2000 ICP-AES spectrometer. Thermogravimetric (TG) analysis was recorded on a Mettler-

Toledo TGA/SDTA 851^c instrument at a heating rate of 10 °C min⁻¹ from 25 to 1000 °C under a flowing N₂ atmosphere. X-ray photoelectron spectra (XPS) were recorded on an Axis Ultra X-ray photoelectron spectrometer. Luminescence spectra were recorded at ambient temperature on an FLS 980 Edinburgh Analytical Instrument apparatus equipped with a 450 W xenon lamp. Photoluminescence (PL) decay lifetimes were measured using a μF900H high-energy microsecond flash lamp as the excitation source.

Synthesis of K₂NaH₅[Eu₄(H₂O)₄W₆(H₆glu)₄O₁₂(B-α-TeW₉O₃₃)₄·60H₂O (1)

K₂TeO₃ (0.400 g, 1.576 mmol) and Na₂WO₄·2H₂O (4.684 g, 14.200 mmol) were added to 20 mL of distilled water. The pH of the solution was adjusted to 2.00 utilizing 6.0 mol L⁻¹ HCl. Then, Eu(NO₃)₃·6H₂O (0.900 g, 2.018 mmol), H₆glu (810 μL, 2.560 mmol) and KCl (1.998 g, 26.800 mmol) were added to the above solution. The pH was adjusted back to 2.00 using 4 mol L⁻¹ NaOH. The final solution was kept in a 90 °C water bath for 2 h and cooled to room temperature and filtered. The filtrate was left to slowly evaporate at room temperature and colorless rod-like crystals were obtained after about 3 days. Yield: 0.87 g (18.89% based on Na₂WO₄·2H₂O). Elemental analysis (%) calcd: C, 2.11; H, 1.25; K, 4.01; W, 56.68; Te, 3.74; Eu, 4.46. Found: C, 1.92; H, 0.88; K, 4.04; W, 51.86; Te, 3.89; Eu, 4.07. IR (KBr, cm⁻¹): 3484 (s), 1640 (s), 1373 (s), 1100 (s), 964 (s), 862 (w), 813 (w), 716 (w).

X-ray crystallography

A suitable single crystal of **1** was sealed in a capillary tube and its intensity data were collected on a Bruker Apex II diffractometer equipped with a bidimensional CCD detector at 296(2) K with graphite monochromated Mo Kα radiation (λ = 0.71073 Å). SADABS-2016/2 was used for absorption correction.¹⁶ Its structure was solved by direct methods and refined on F² by full-matrix least-squares method using the SHELXTL-2018 program package and the Olex-2 software.¹⁷ Lorentz polarization and SADABS corrections were applied. All H atoms connected to N and C atoms were generated geometrically and refined isotropically. No hydrogen atoms attached to water molecules were located from the difference Fourier map. For **1**, the checkcif report shows there are still solvent-accessible voids, implying the existence of some solvent molecules and counter cations in the structure that cannot be found from the weak residual electron peaks. These solvent molecules and counter cations are highly disordered. The solvent mask instruction was further used to calculate and evaluate the possible numbers of the disordered solvent water molecules and cations in the accessible voids of the crystal structure. The solvent mask result indicates that *ca.* 617 electrons are located in a void of 3498.5 Å³ for each molecular unit of **1**. Thus, another 44 water molecules and 12 K⁺ cations were directly added to the molecular formula according to the elemental analyses, TG analysis and the solvent mask result. Crystallographic data and structural refinements for **1** are sum-

marized in Table S1.† CCDC 1936173 contains the supplementary crystallographic data for **1**.†

FL sensing

1.0 mg of **1** as a powder was dissolved in 1.0 mL of aqueous solution, then ultrasonicated for 5 min to allow the powder to dissolve completely and allowed to stand for 10 h to obtain a stable solution of **1**. After the addition of the analyte, the excitation, emission spectra and life decay curves were recorded under excitation at 394 nm (excitation slit = 4 nm, emission slit = 4 nm). Each measurement was repeated three times. The change in the emission intensity at 614 nm was subjected to linear discriminant analysis.

Results and discussion

Structural description

The powder X-ray diffraction (PXRD) pattern of **1** is consistent with the simulated PXRD pattern from the single-crystal X-ray structural analysis, indicating that the sample of **1** is pure (Fig. S1†).

1 crystallizes in the hexagonal space group P6₁ (Table S1†) and its molecular structure consists of an unprecedented gluconic acid ligand connected multi-Eu^{III}-incorporated TT [Eu₄(H₂O)₄W₆(H₂glu)₄O₁₂(B-α-TeW₉O₃₃)₄]²⁴⁻ (**1a**) anion (Fig. 1a),

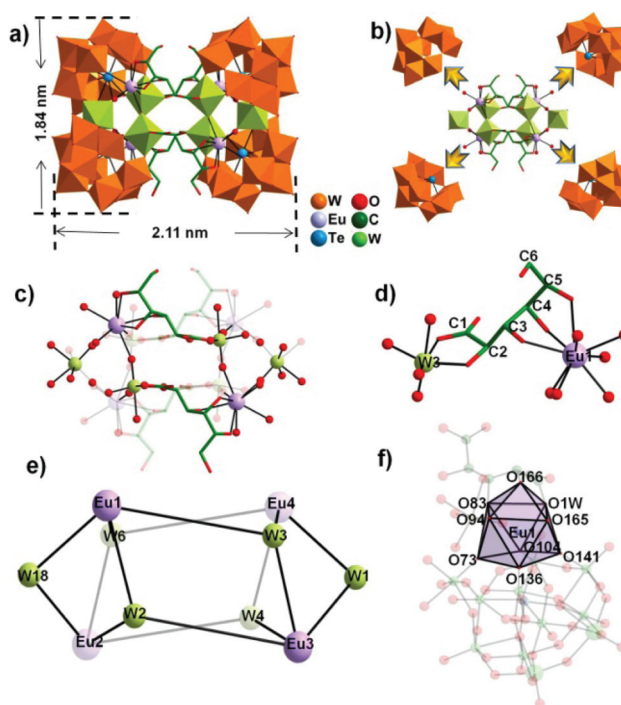


Fig. 1 (a) View of the tetrameric **1a** POA. (b) Combination of four trivalent Keggin [B-α-TeW₉O₃₃]⁸⁻ segments with a heterometallic **1b** cluster. (c) View of the **1b** cluster. (d) View of the [Eu₁(H₂O)W₃(H₂glu)O₂]⁺ entity highlighting the flexible polyhydroxycarboxylic coordination mode of a H₂glu⁴⁻ ligand. (e) Simplified view of the **1b** cluster. (f) The distorted monocationic square antiprismatic geometry of the Eu¹³⁺ ion.

14 K⁺ cations, 10 protons and 60 lattice water molecules. This interesting polyhydroxycarboxylic acid ligand bridged tetrameric **1a** polyoxoanion (POA) with dimensions of about 2.11 × 1.84 nm can be considered as an aggregation of four trivalent Keggin [B-α-TeW₉O₃₃]⁸⁻ fragments and an unseen heterometallic [Eu₄(H₂O)₄W₆(H₂glu)₄O₁₂]⁸⁺ (**1b**) cluster (Fig. 1b). The trivalent Keggin [B-α-TeW₉O₃₃]⁸⁻ fragment can be regarded as removing a {W₃O₁₃} triad from the hypothetical Keggin [α-TeW₁₂O₄₀]⁴⁻ POA. The difference between the two isomers [B-α-TeW₉O₃₃]⁸⁻ and [B-β-TeW₉O₃₃]⁸⁻ is that one edge-sharing {W₃O₁₃} triad clockwise is rotated 60° among the three {W₃O₁₃} triads (Fig. S2[†]). In four [B-α-TeW₉O₃₃]⁸⁻ segments, all the Te heteroatoms display a triangular pyramid geometry with Te–O bond lengths of 1.852(14)–1.911(18) Å and O–Te–O angles of 88.6(6)–98.6(8)°. All the W atoms exhibit an octahedral configuration with W–O distances of 1.664(14)–2.490(16) Å and O–W–O bond angles of 69.5(6)–176.0(8)°. Notably, the heterometallic **1b** cluster can be further divided into a [Eu₄(H₂O)₄W₆(H₂glu)₄O₈]⁴⁺ central core and two bridging {WO₆} groups on both sides (Fig. 1c, Fig. S3[†]). Upon scrupulous inspection, it can be clearly seen that the [Eu₄(H₂O)₄W₆(H₂glu)₄O₈]⁴⁺ central core comprises four identical [Eu(H₂O)W(H₂glu)O₂]⁺ entities, in which extraneous W^{VI} and Eu^{III} centers are combined with each other through H₂glu⁴⁻ ligands. Taking the [Eu1(H₂O)W3(H₂glu)O₂]⁺ entity established by the Eu1 and W3 centers as an example to describe the coordination environment of the H₂glu⁴⁻ ligand (Fig. 1d), the terminal carboxyl group and the orthohydroxyl group of the H₂glu⁴⁻ ligand chelate with the W3 center, whereas the hydroxyl groups linking the C3, C4 and C5 atoms directly coordinate to the Eu1 center. The remaining three H₂glu⁴⁻ ligands are respectively combined with Eu2 and W4, Eu3 and W2, and Eu4 and W6 centers (Fig. S4[†]). It is worth mentioning that this is the first time that a multiple hydroxyl coordination mode of the H₂glu⁴⁻ ligand has been observed in POM chemistry. In addition, it should be noted that the Eu1 and W6, Eu2 and W2, Eu3 and W4, Eu4 and W3 centers in the **1b** cluster are linked together by sharing μ₂-O atoms from extraneous {WO₆} octahedra, giving rise to a bicapped square prism distribution mode (Fig. 1e). Besides this, the four crystallographically independent Eu³⁺ ions have similar coordination environments and all display a distorted monocapped square antiprism geometry (Fig. 1f, Fig. S5[†]). Thus, only the Eu1³⁺ ion is described here. The coordination sphere of the Eu1³⁺ cation is defined by five μ₂-O atoms from five {WO₆} octahedra [Eu–O: 2.351(14)–2.561(14) Å], three μ₂-O atoms from one H₂glu⁴⁻ ligand [Eu–O: 2.476(18)–2.493(15) Å] and a terminal water ligand [Eu–O: 2.398(16) Å]. Among five μ₂-O atoms from five {WO₆} octahedra, the O136 and O141 atoms come from a trivalent [B-α-TeW₉O₃₃]⁸⁻ fragment [Eu1–O136: 2.418(16) Å, Eu1–O141: 2.436(16) Å], the O104 atom is from a bridging {WO₆} octahedron [Eu1–O104: 2.351(14) Å], and the O73 and O83 atoms originate from the {WO₆} octahedron linking the terminal carboxyl group of H₂glu⁴⁻ ligand [Eu1–O73: 2.561(14) Å, Eu1–O83: 2.445(13) Å]. In the distorted monocapped square antiprism, the O73, O104, O136 and O141

atoms constitute the bottom plane whereas the top plane is formed by the O1 W, O83, O94 and O165 atoms. Note that the O166 atom from the H₂glu⁴⁻ ligand occupies the capping site of the square antiprism, which greatly impairs the quenching effect from the O–H oscillation and suggests the potential of **1** for sensing trace analytes in water sources.

In addition to the tetrameric POA of **1**, other tetrameric POAs of TTs have been also reported. For example, in 2018, Hu and collaborators reported two new-fashioned tetrameric RE-containing POAs [{RE(H₂O)₅(Te^{VI}W₁₈O₆₄)₄]⁴⁴⁻ (RE = Eu³⁺, Gd³⁺) (Fig. 2a) grown from the filtrate of [(WO₂){RE(H₂O)₅(Te^{VI}W₁₈O₆₅)₂]²⁴⁻ in a refrigerator (10 °C), which were formed from four corner-sharing mono-RE substituted Dawson-like [RETe^{VI}W₁₈O₆₄]¹¹⁻ fragments through the coordination of each RE cation with two lacunary oxygen atoms from one [Te^{VI}W₁₈O₆₄]¹⁴⁻ fragment, two terminal oxygen atoms from the other adjacent [Te^{VI}W₁₈O₆₄]¹⁴⁻ fragment, with the four RE cations arranged in a square motif (Fig. 2b).¹⁸ These represent the largest TTs(vi) reported to date. In 2017, our group communicated the first 2-picolinic-acid decorated tetrameric RECTTs [RE₂(H₂O)₄(pica)₂W₂O₅[(RE(H₂O)W₂(Hpica)₂O₄)(B-β-Te^{IV}W₈O₃₀H₂)₂]²⁴⁻ (RE = La³⁺, Ce³⁺, Nd³⁺, Sm³⁺, Eu³⁺) (Fig. 2c), which can be imagined as a combination of four tetravalent Keggin [B-β-Te^{IV}W₈O₃₀H₂]⁶⁻ segments pocketing an inorganic–organic hybrid RE–TM heterometallic species {[RE₂(H₂O)₄(pica)₂W₂O₅[(RE(H₂O)W₂(Hpica)₂O₄)]₂]²⁰⁺ (Fig. 2d).⁷ In the same year, the first organotin–RE heterometallic TTs {[[Sn(CH₃)₂W₂O₄(IN)][(B-α-Te^{IV}W₈O₃₁)RE(H₂O)(Ac)]₂]₂]²⁰⁻ (RE = Ce³⁺, Pr³⁺, Nd³⁺, Sm³⁺, Eu³⁺, Gd³⁺, Tb³⁺) (Fig. 2e) were triumphantly isolated by our group in the acid aqueous medium with the addition of [(CH₃)₂Sn]²⁺ electrophile, dimethylamine hydrochloride, acetic acid and HIN organic solubilizers. The unique tetrameric POAs are constructed from four [B-α-Te^{IV}W₈O₃₁]¹⁰⁻ subunits, two dimethylated [Sn(CH₃)₂]³⁺ groups and one unique inorganic–organic linear-shaped {[W₂O₄(IN)][(RE(H₂O)(Ac)]₂]₂]¹⁴⁺ cluster (Fig. 2f).⁸ Moreover, by adjusting the pH of the reaction solution to 7.0, an unexpected Te^{IV}-bridged tetrameric aggregate [W₂₈Te^{IV}O₁₁₂]²⁴⁻ was successfully assembled by Cronin's group (Fig. 2g), in which not only the {TeO₃} groups participate in the fabrication of the pentavalent Keggin [TeW₇O₂₈]¹⁰⁻ subunits but also the {TeO₄} groups in the square arrangement mode bridge adjacent [TeW₇O₂₈]¹⁰⁻ subunits (Fig. 2h).^{19a} In addition, in 2018, Cronin's group discovered an excellent self-sorting cross-shaped tetrameric POA [H₄P₄Te^{IV}W₆₄O₂₂₄]³¹⁻ using two different heteroanion templates (Fig. 2i),^{19b} which can be reasonably described as the cleavage of four uncommon trivalent Dawson heteroanion [P^{III}Te^{IV}W₁₅O₅₄]¹¹⁻ subunits and four {WO₆} bridges (Fig. 2j). It can be markedly seen from the above comparison that poly(TT) aggregates can display diverse architectures with the participation of RE ions, organometal groups, different heteroatoms, additional {WO₆} linkers and functional organic components, which provide us with great opportunities to continuously explore and develop this attractive area in time.

From another point of view, it is extremely intriguing that **1a** is also considered as a fusion of two dimeric

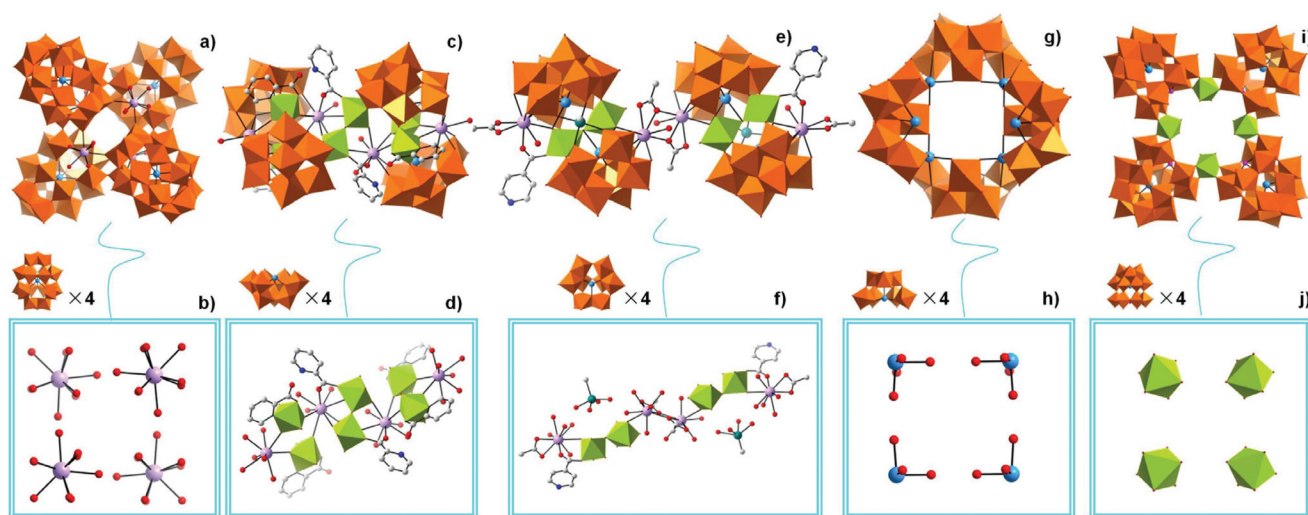


Fig. 2 (a–b) View of the tetrameric $\{[\text{RE}(\text{H}_2\text{O})_5(\text{Te}^{\text{VI}}\text{W}_{18}\text{O}_{64})]_4\}^{44-}$ POA and the distribution of four RE bridges in it.¹⁸ (c–d) View of the tetrameric $[\text{Nd}_2(\text{H}_2\text{O})_4(\text{pica})_2\text{W}_2\text{O}_5][(\text{Nd}(\text{H}_2\text{O})\text{W}_2(\text{Hpica})_2\text{O}_4)(\text{B}-\beta\text{-TeW}_8\text{O}_{30}\text{H}_2)]_2^{24-}$ POA and the RE–TM heterometallic $\{[\text{RE}_2(\text{H}_2\text{O})_4(\text{pica})_2\text{W}_2\text{O}_5][(\text{RE}(\text{H}_2\text{O})\text{W}_2(\text{Hpica})_2\text{O}_4)]_2\}^{20+}$ cluster in it.⁷ (e–f) View of the tetrameric $\{[\text{Sn}(\text{CH}_3)_3\text{W}_2\text{O}_4(\text{IN})][(\text{B}-\alpha\text{-TeW}_8\text{O}_{31})\text{RE}(\text{H}_2\text{O})(\text{Ac})_2]_2\}^{20-}$ POA and the distribution of two $[\text{Sn}(\text{CH}_3)_3]^{3+}$ groups and the inorganic–organic linear-shaped $\{[\text{W}_2\text{O}_4(\text{IN})][\text{RE}(\text{H}_2\text{O})(\text{Ac})_2]_2\}^{14+}$ cluster in it.⁸ (g–h) View of the tetrameric $[\text{W}_{28}\text{Te}_8\text{O}_{112}]^{24-}$ POA and four $\{\text{TeO}_4\}$ linkers in the square arrangement mode.^{19a} (i–j) View of the self-sorting cross-shaped tetrameric $[\text{H}_4\text{P}_4\text{Te}_4\text{W}_{64}\text{O}_{224}]^{31-}$ POA and the distribution of the four $\{\text{WO}_6\}$ linkers in it.^{19b}

$[\text{Eu}_2(\text{H}_2\text{O})_2\text{W}_3\text{O}_6(\text{B}-\alpha\text{-TeW}_9\text{O}_{33})_2]^{4-}$ moieties by means of the bridging function of four $\text{H}_2\text{glu}^{4-}$ ligands (Fig. 3a, Fig. S6a†). Notably, the $[\text{Eu}_2(\text{H}_2\text{O})_2\text{W}_3\text{O}_6(\text{B}-\alpha\text{-TeW}_9\text{O}_{33})_2]^{4-}$ subunit (Fig. 3b) can be thought of as an openmouthed $[\text{Te}_2\text{W}_{19}\text{O}_{68}]^{8-}$ segment (Fig. 3c) that embraces a tetra-nuclear $[\text{Eu}_2(\text{H}_2\text{O})_2\text{W}_2\text{O}_4]^{10+}$ cluster (Fig. 3d). The openmouthed $[\text{Te}_2\text{W}_{19}\text{O}_{68}]^{8-}$ segment is constructed from two trivalent Keggin $[\text{B}-\alpha\text{-TeW}_9\text{O}_{33}]^{8-}$ fragments sharing a bridging $\{\text{WO}_6\}$ octahedron through four oxygen atoms from two $[\text{B}-\alpha\text{-TeW}_9\text{O}_{33}]^{8-}$ fragments, with an openmouthed angle of 65.9° .

The openmouthed pocket of the $[\text{Te}_2\text{W}_{19}\text{O}_{68}]^{8-}$ segment provides an excellent opportunity for encapsulating other extraneous metal centers. Herein, two W and two Eu centers are encapsulated in the openmouthed pocket, giving rise to the $[\text{Eu}_2(\text{H}_2\text{O})_2\text{W}_3\text{O}_6(\text{B}-\alpha\text{-TeW}_9\text{O}_{33})_2]^{4-}$ subunit (Fig. 3b). In one tetra-nuclear $[\text{Eu}_2(\text{H}_2\text{O})_2\text{W}_2\text{O}_4]^{10+}$ cluster (Fig. 3d), Eu1, W2, Eu2 and W6 centers are combined with each other *via* O atoms to form a distorted square (Fig. 3e). The distances of Eu1–W2, Eu1–W6, Eu2–W2 and Eu2–W6 are 4.115(6), 4.256(8) and 4.099(4) Å, respectively. Besides this, the W18 bridge links to Eu1 and Eu2 centers, where the distances between the bridging W18 center and Eu^{3+} ions vary from 4.122(9) to 4.135(2) Å (Eu1–W18: 4.122(9), Eu2–W18: 4.135(2) Å) (Fig. 3f). In the other tetra-nuclear $[\text{Eu}_2(\text{H}_2\text{O})_2\text{W}_2\text{O}_4]^{10+}$ cluster (Fig. S6b and c†), the Eu3, W1, Eu4 and W3 centers are interconnected by O atoms to form a distorted square motif (Fig. S6d†). The distances of Eu3–W4, Eu3–W3, Eu4–W4 and Eu4–W3 are 4.237(4), 4.149(5), 4.133(4) and 4.234(8), respectively (Fig. S6e†). The W1 bridge links to Eu3 and Eu4 centers and the distances between the bridging W1 center and Eu^{3+} ions are in the range of 4.106(4)–4.117(9) Å [Eu3–W1: 4.117(9), Eu4–W1: 4.106(4) Å] (Fig. S6f†).

Furthermore, the most intriguing structural feature of **1** is that each **1a** POA (Fig. S7†) interacts with three K^+ cations and each K^+ cation interacts with three **1a** POAs, resulting in a unique 3D (3,3)-connected supramolecular framework with a Schafli symbol of $(8^3)(8^3)$, in which **1a** and K^+ ions act as 3-connected nodes (Fig. 4a and b). Noticeably, the regular alignments of **1a** and K^+ linkers along the 6_1 screw axis give rise to a helical channel A with cross-section dimensions of $9.0 \times 9.0 \text{ \AA}^2$ (Fig. 4c and d, Fig. S8†). Besides this, two adjacent left-

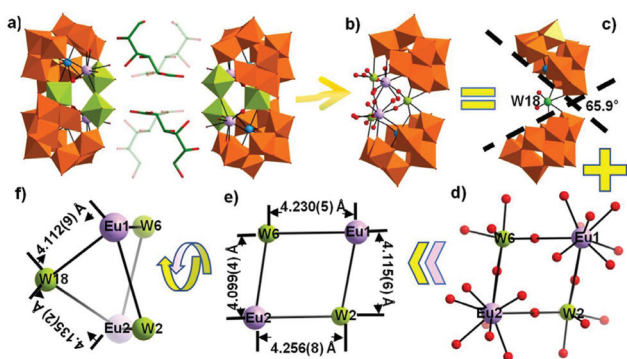


Fig. 3 (a) The combination of two $[\text{Eu}_2(\text{H}_2\text{O})_2\text{W}_3\text{O}_6(\text{B}-\alpha\text{-TeW}_9\text{O}_{33})_2]^{4-}$ subunits and four $\text{H}_2\text{glu}^{4-}$ linkers. (b) A dimeric $[\text{Eu}_2(\text{H}_2\text{O})_2\text{W}_3\text{O}_6(\text{B}-\alpha\text{-TeW}_9\text{O}_{33})_2]^{4-}$ subunit containing W2, W6, Eu1 and Eu2 centers. (c) An openmouthed $[\text{Te}_2\text{W}_{19}\text{O}_{68}]^{8-}$ segment containing a W18 bridge. (d) Top view of a tetra-nuclear $[\text{Eu}_2(\text{H}_2\text{O})_2\text{W}_2\text{O}_4]^{10+}$ cluster constructed from W2, W6, Eu1 and Eu2 atoms. (e) A simplified view of the $[\text{Eu}_2(\text{H}_2\text{O})_2\text{W}_2\text{O}_4]^{10+}$ cluster. (f) Side view of the simplified $[\text{Eu}_2(\text{H}_2\text{O})_2\text{W}_3\text{O}_6]^{12+}$ cluster.

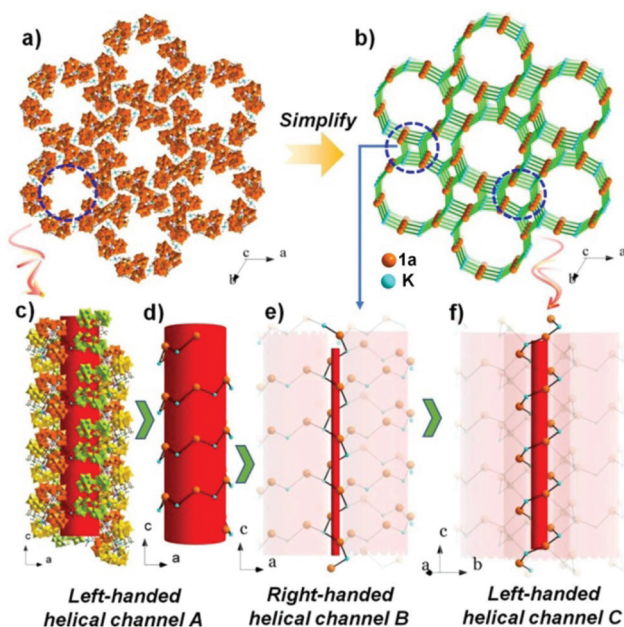


Fig. 4 (a) The 3D supramolecular framework of **1** along the *c* axis. (b) The 3D topological framework viewed along the *c* axis. (c) View of the left-handed helical chain A constructed from six **1a** POAs and six K^+ linkers. (d) View of the simplified left-handed helical chain A. (e) The simplified 3D right-handed helical channel B between two helical channels A. (f) The simplified 3D left-handed helical channel C surrounded by three A and three B channels. Color code: the yellow spheres represent the **1a** polyanions and the turquoise spheres represent K^+ cations.

handed A helical channels are further combined with each other by K^+ cations and **1a** POAs, creating a right-handed B helical channel (Fig. 4e, Fig. S9†). Simultaneously, three left-handed A helical channels and three right-handed B helical channels are further interlinked to construct a left-handed C helical channel along the *c* axis (Fig. 4f, Fig. S10†). The hexagonal array of **1a** POAs along the *c* axis provides excellent porous channels to be filled by solvent molecules, which greatly increases the specific surface area of the whole framework and is benefit for FL sensing in aqueous solution.

IR spectra

In the low wavenumber region ($\nu < 1000 \text{ cm}^{-1}$) of **1**, the characteristic stretching absorption bands originating from the Keggin TT skeleton are prominently observed (Fig. S11a†). Referring to the IR spectrum of $K_2\text{TeO}_3$, the vibration peak at 710 cm^{-1} can be attributed to the stretching vibration mode of $\nu(\text{Te-O})$. Specifically, the vibrational peaks at 963, 860 and 788 cm^{-1} can be assigned to the stretching vibration modes of $\nu(\text{W-O}_t)$, $\nu(\text{W-O}_b)$ and $\nu(\text{W-O}_c)$, respectively.^{8,18,20} In the high wavenumber range ($\nu > 1000 \text{ cm}^{-1}$), the $\nu(\text{C-O})$ stretching vibration is observed at 1094 cm^{-1} . Besides this, the symmetrical stretching vibration of the carboxylic group of H_6glu appears at 1361 cm^{-1} , whereas the asymmetric stretching vibration of the carboxylic group of the H_6glu is seen at 1633 cm^{-1} . Actually, the stretching vibration band at 1633 cm^{-1} also contains the bending vibration of a $\nu(\text{O-H})$

group of water molecules. As discussed in previous reports, the separation (Δ) between the asymmetric stretching vibration and symmetric stretching vibration of the carboxylic group could distinguish the coordination mode of a carboxyl group.^{4c,21} When a carboxyl group adopts a chelating or bridging mode, Δ is lower than 200 cm^{-1} because the symmetric and asymmetric vibrations arise in the same direction, in contrast, the monodentate coordination of a carboxyl group will sharply increase the asymmetric stretching vibration, with Δ higher than 260 cm^{-1} .²² The Δ value in the IR spectrum (272 cm^{-1}) of **1** is larger than 260 cm^{-1} , which indicates that the carboxyl group of H_6glu is monodentate. Moreover, the intense peak at 3453 cm^{-1} can be attributed to the stretching vibration of the $\nu(\text{O-H})$ groups of H_6glu and water molecules.²³

Thermogravimetric (TG) analysis

It can be seen from Fig. S11b† that the weight loss of **1** can be divided into two steps. When the heating temperature reaches $250 \text{ }^\circ\text{C}$, the first-step weight loss of 8.07% (calcd. 7.92%) corresponds to the liberation of 60 lattice water molecules. With an increase in the temperature, the second-step weight loss of 13.56% (calcd. 13.67%) up to $700 \text{ }^\circ\text{C}$ can be attributed to the loss of four coordination water molecules, four organic ligands, the dehydration of protons, the decomposition of the remaining organic ligands, as well as the sublimation of four WO_3 , which led to the collapse of the POA skeleton of **1**.⁸

Solid-state FL properties of **1**

RE-containing materials exhibit various promising applications as biomarkers, drug carriers and optical sensors because of the narrow emission lines and high colour purity derived from transitions inside the 4f shell of the RE^{3+} ions, especially for Eu^{3+} -based materials with stable emission bands and long FL lifetimes.^{3,6} To better understand the FL properties of **1**, the solid-state emission spectrum was recorded at an excitation wavelength of 394 nm, revealing five characteristic emission bands at 579, 594, 614, 650 and 701 nm in the range of 500–750 nm, which can be respectively attributed to the $\text{Eu}^{3+} \text{ } ^5\text{D}_0 \rightarrow ^7\text{F}_0$, $^5\text{D}_0 \rightarrow ^7\text{F}_1$, $^5\text{D}_0 \rightarrow ^7\text{F}_2$, $^5\text{D}_0 \rightarrow ^7\text{F}_3$ and $^5\text{D}_0 \rightarrow ^7\text{F}_4$ transitions (Fig. 5a).²⁴ When the 614 nm emission was monitored, its excitation spectrum was also collected, in which five peaks at 362, 379, 394, 415 and 465 nm were respectively observed that correspond to the $^7\text{F}_0 \rightarrow ^5\text{D}_4$, $^7\text{F}_0 \rightarrow ^5\text{G}_2$, $^7\text{F}_0 \rightarrow ^5\text{L}_6$, $^7\text{F}_0 \rightarrow ^5\text{D}_3$ and $^7\text{D}_0 \rightarrow ^5\text{D}_2$ transitions of the Eu^{3+} ions (Fig. 5b) and a strong broad excitation band centered at 275 nm stemming from the $^1\text{A}_{1g} \rightarrow ^1\text{T}_{1u}$ transition of the O \rightarrow W LMCT of the TT fragments (see the inset in Fig. 5b).^{5a,24} The appearance of the broad excitation band stemming from the $^1\text{A}_{1g} \rightarrow ^1\text{T}_{1u}$ transition of the O \rightarrow W LMCT of TT fragments in the excitation spectrum monitored by the most intense emission at 614 nm of the Eu^{3+} ions in some degree demonstrates the occurrence of energy transfer from TT fragments to Eu^{3+} ions. The lifetime decay profile of **1** was obtained by monitoring the most intense emission at 614 nm (Fig. 5c), which obeys a second-order exponential function:

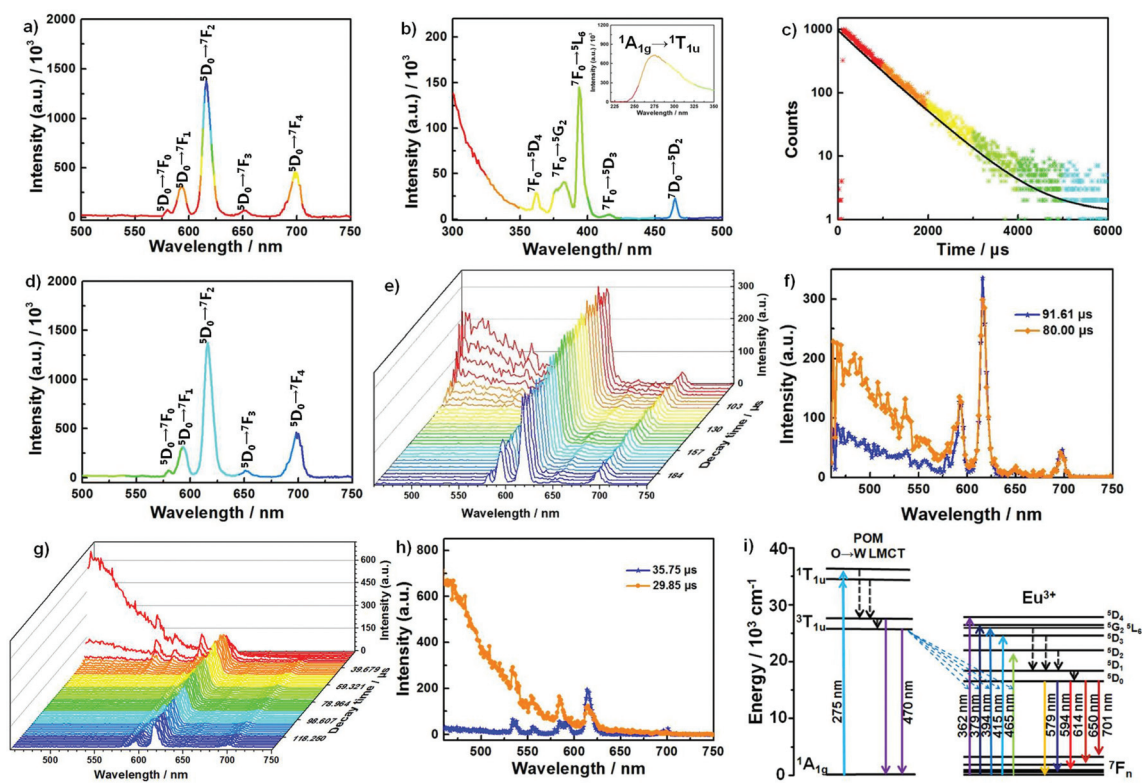


Fig. 5 (a) The solid-state emission spectrum of **1** under excitation at 394 nm. (b) The solid-state excitation spectrum of **1** taken by monitoring the strongest emission at 614 nm. (c) The solid-state lifetime decay curve of **1** obtained by monitoring the strongest emission at 614 nm. (d) The solid-state emission spectrum of **1** under excitation at 275 nm. (e) The TRES of **1** in the range of 80 to 200 μs under excitation at 394 nm. (f) The emission spectra of **1** at decay times of 80.00 and 91.61 μs under excitation at 394 nm. (g) The TRES of **1** in the range of 22.00 to 132.00 μs under excitation at 275 nm. (h) The emission spectra of **1** at the decay times of 29.85 and 35.75 μs under excitation at 275 nm. (i) The energy level diagram of **1** presenting the intramolecular energy transfer from TT fragments to Eu^{3+} ions.

$I = A_1 \exp(-t/\tau_1) + A_2 \exp(-t/\tau_2)$. The fitting lifetimes are $\tau_1 = 379.17 \mu\text{s}$ (8.45%) and $\tau_2 = 711.83 \mu\text{s}$ (91.55%) and the pre-exponential factors are $A_1 = 145.57$ and $A_2 = 840.13$. Therefore, the average decay time (τ^*) can be determined using the formula: $\tau^* = (A_1\tau_1^2 + A_2\tau_2^2)/(A_1\tau_1 + A_2\tau_2)$, which is calculated to be 683.71 μs .^{7,24}

Moreover, to demonstrate the existence of energy transfer from TT fragments to Eu^{3+} ions, the emission spectrum of **1** was also collected under $\text{O} \rightarrow \text{W}$ LMCT excitation at 275 nm of the TT segments (Fig. S12[†]), which exhibits the similar characteristic emission bands of Eu^{3+} ions to those observed under the $\text{Eu}^{3+} {}^7\text{F}_0 \rightarrow {}^5\text{L}_6$ excitation at 394 nm (Fig. 5d). The time-resolved emission spectrum (TRES) of **1** was recorded in the range of 460–750 nm with an interval of 2 nm under excitation at 394 nm. When sliced in the range of 80–200 μs , the TRES of **1** firstly exhibits a typical ${}^3\text{T}_{1u} \rightarrow {}^1\text{A}_{1g}$ broad emission band at 470 nm derived from the $\text{O} \rightarrow \text{W}$ LMCT of the TT fragments. As time goes on, the ${}^3\text{T}_{1u} \rightarrow {}^1\text{A}_{1g}$ broad emission band presents a rapid attenuating trend, but the intensity of the emission bands of the Eu^{3+} ions decreases very slowly in the range of 80–200 μs (Fig. 5e). The decay of the ${}^3\text{T}_{1u} \rightarrow {}^1\text{A}_{1g}$ emission of the TT fragments is more rapid than that of the Eu^{3+} emission peaks, which reveals the occurrence of energy migration from

the TT fragments to Eu^{3+} cations in which the TT fragments sensitize the Eu^{3+} emission and suppress the decay of the emission intensity of the Eu^{3+} cations. This energy migration phenomenon has been observed by Yamase *et al.* in studies on polyoxometalloeuropates such as $\text{Na}_9[\text{EuW}_{10}\text{O}_{36}] \cdot 32\text{H}_2\text{O}$,^{25a} $\text{K}_{15}\text{H}_3[\text{Eu}_3(\text{H}_2\text{O})_3(\text{SbW}_9\text{O}_{33})(\text{W}_5\text{O}_{18})_3] \cdot 25.5\text{H}_2\text{O}$,^{25b} and $[\text{Eu}(\text{H}_2\text{O})_8]_3\text{K}_2\text{H}_3[(\text{GeTi}_3\text{W}_9\text{O}_{37})_2\text{O}_3] \cdot 13\text{H}_2\text{O}$.^{25c} In fact, Yamase, Hill, Francesconi and Boskovic have already investigated the use of POMs as antennae for the sensitization of RE elements and the energy transfer mechanism.^{5,8,18,25} In our findings, it can be apparently seen from the slice map of the TRES of **1** (Fig. 5f) that the intensity of the ${}^3\text{T}_{1u} \rightarrow {}^1\text{A}_{1g}$ broad emission band declines while the intensity of the emission bands of the Eu^{3+} ions slightly rise in the process of the decay time, varying from 80.96 to 91.96 μs , which directly attests the occurrence of energy migration from the TT fragments to Eu^{3+} ions in **1**. Furthermore, the TRES of **1** under $\text{O} \rightarrow \text{W}$ LMCT excitation at 275 nm of the TT segments was also measured (Fig. 5g), in which the phenomenon that the ${}^3\text{T}_{1u} \rightarrow {}^1\text{A}_{1g}$ broad emission band quickly disappears whereas the intensity of the emission bands of the Eu^{3+} ions slowly decrease was also observed. Meanwhile, the slice map of the TRES of **1** obtained under $\text{O} \rightarrow \text{W}$ LMCT excitation (Fig. 5h) also indicates that the emis-

sion intensity of the Eu^{3+} ions slightly increases when the ${}^3\text{T}_{1\text{u}} \rightarrow {}^1\text{A}_{1\text{g}}$ emission intensity weakens in the process of the decay time varying from 29.85 to 35.75 μs , which explicitly manifests the occurrence of energy transfer from the TT fragments to the Eu^{3+} ions in 1.

Based on the above analysis, the luminescence mechanism diagram of 1 was devised and is proposed in Fig. 5i. The luminescence process is as follows. When 1 is excited, some of the light is absorbed by the Eu^{3+} ions, which leads to the f-f ${}^5\text{D}_0 \rightarrow {}^7\text{F}_0$, ${}^5\text{D}_0 \rightarrow {}^7\text{F}_1$, ${}^5\text{D}_0 \rightarrow {}^7\text{F}_2$, ${}^5\text{D}_0 \rightarrow {}^7\text{F}_3$ and ${}^5\text{D}_0 \rightarrow {}^7\text{F}_4$ emissions. At the same time, some of the light is absorbed by the TT fragments and pumps the electrons in the TT fragments from the ground state ${}^1\text{A}_{1\text{g}}$ to the excited state ${}^1\text{T}_{1\text{u}}$. Due to the spin-orbital coupling interaction, the electrons relax from the ${}^1\text{T}_{1\text{u}}$ state to the ${}^3\text{T}_{1\text{u}}$ state by undergoing a non-radiative process. Subsequently, when the electrons in the TT fragments return to the ground state from the excited state ${}^3\text{T}_{1\text{u}}$, most of the electrons are trapped by the Eu^{3+} ions. The trapped electrons can be absorbed by the ground state of the Eu^{3+} ions, promoting energy transfer from the TT fragments to the Eu^{3+} ions and sensitizing the emission of the Eu^{3+} ions. The stable and unique FL properties of 1 urge us to investigate its potential applications.

FL properties and stability of 1 in aqueous solution

Up to now, FL sensors for detecting trace substances have aroused widespread interest on account of their high sensitivity and selectivity.² Therefore, we decided to use 1 to construct a FL sensor for detecting Cu^{2+} ions in aqueous solution. It is well known that the excellent detection performance of a FL sensor is highly dependent on the emission properties and stability of the sensor. Thus, the emission spectrum of 1 in aqueous solution was collected in the range of 500–750 nm under excitation at 394 nm (Fig. S13a†), which displayed five obvious characteristic emission bands at 579, 594, 614, 650 and 701 nm from the Eu^{3+} ${}^5\text{D}_0 \rightarrow {}^7\text{F}_0$, ${}^5\text{D}_0 \rightarrow {}^7\text{F}_1$, ${}^5\text{D}_0 \rightarrow {}^7\text{F}_2$, ${}^5\text{D}_0 \rightarrow {}^7\text{F}_3$ and ${}^5\text{D}_0 \rightarrow {}^7\text{F}_4$ transitions, which is consistent with the solid-state emission spectrum of 1, manifesting that the POA skeleton structure of 1 may be stable in aqueous solution and is suitable to act as a FL probe to detect metal cations in aqueous solution.²⁴ The emission band at 614 nm is the most intense, which can be used as the detection signal of the sensor based on 1.²⁶

In order to further examine the stability of the POA skeleton structure of 1 in aqueous solution, its ${}^{125}\text{Te}$ NMR spectrum was measured in D_2O (Fig. S14†), which exhibits a single resonance signal at $\delta = -1796.77$ ppm in the range of 1580–2040 ppm that can be assigned to the Te^{IV} center in the trivacant Keggin $[\text{B}-\alpha\text{-TeW}_9\text{O}_{33}]^{8-}$ fragments in 1. This observation indicates that the POA skeleton structure of 1 is stable in aqueous solution. The experimental result of the ${}^{125}\text{Te}$ NMR spectrum of 1 is consistent with the reported literature from Boskovic's group.²⁷ Furthermore, we collected the FL emission spectra of 1 in aqueous solution (1.0 mg mL^{-1}) under different pH values adjusted using diluted hydrochloric acid and sodium hydroxide solution. This was done because the magne-

todipolar ${}^5\text{D}_0 \rightarrow {}^7\text{F}_{1,3}$ emissions are not sensitive to the local coordination environment of the Eu^{3+} ion and their emission intensities are almost unchanged upon the variation in the local coordination environment of the Eu^{3+} ion whereas the electro-dipolar ${}^5\text{D}_0 \rightarrow {}^7\text{F}_{0,2,4}$ emissions are extremely sensitive to the local coordination environment and a minor change in the local coordination environment of the Eu^{3+} ion leads to remarkable variation in the ${}^5\text{D}_0 \rightarrow {}^7\text{F}_{0,2,4}$ emissions.^{24,26} Under excitation at 394 nm, the emission spectrum of 1 in aqueous solution (pH = 4.63) shows five characteristic peaks of the Eu^{3+} ions (Fig. 6a and b), where the emission peak intensity slightly varies when the pH changes from 2.02 to 9.91. However, when the pH is lower than 2.02, the emission intensity sharply attenuates, which indicates that the skeleton structure of 1 begins to change. Similarly, the emission intensity also gradually declines when the pH is higher than 9.91, suggesting that the skeleton structure of 1 begins to change. It can be concluded that the skeleton structure of 1 is stable in the pH range of 2.02–9.91. Meanwhile, UV-vis spectroscopy can be used as an effective method to investigate the stability of a compound in aqueous solution, according to the previous literature.^{28,29a} Thus, the UV spectra of 1 in aqueous solution with different pH values were also measured. As shown in Fig. 6c and d, the strong absorption band at about 192 nm can be attributed to the $\text{p}\pi\text{-d}\pi$ charge-transfer transitions of the $\text{O}_\text{t} \rightarrow \text{W}$ bonds and the weak absorption band at *ca.* 270 nm can be assigned to the $\text{p}\pi\text{-d}\pi$ charge-transfer transitions of the $\text{O}_{\text{b(c)}} \rightarrow \text{W}$ bonds.²⁹ When the pH is lower than 2.00 or higher than 9.99, the absorption band at *ca.* 270 nm gradually becomes weaker until it disappears and the absorption band at *ca.* 192 nm becomes stronger and blue-shifted. Evidently, the UV spectra of 1 basically remain unchanged in the pH range of 2.00–9.99, which suggests that the POA skeleton struc-

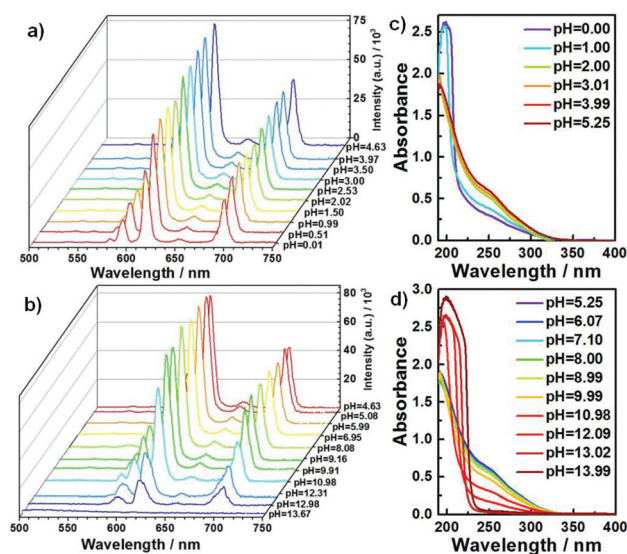


Fig. 6 (a–b) Evolution of the FL emission spectra of 1 in aqueous acidic and alkaline solutions. (c–d) Evolution of the UV spectra of 1 in aqueous acidic and alkaline solutions.

ture of **1** is stable in the pH range of 2.00–9.99. This result is in good agreement with the FL emission spectra. Moreover, as Cronin depicted, electrospray ionization mass spectrometry (ESI-MS) can be a highly effective tool to probe the stability of the cluster species in solution, the intrinsic charge and the characteristic isotopic envelopes captured by ESI-MS can be precisely fitted to determine the exact formula of a material.^{28a,30} Thus, the ESI-MS measurements of **1** in aqueous solution were conducted. As shown in Fig. 7a and b, there are a series of charged peaks in the region of 1400–4000 m/z and the assignments of these characteristic charged peaks to the corresponding POA fragments are provided in Table S2 (Fig. S15†). The main peak ($m/z = 1510.32$) with a charge of -8 corresponds to the $\{[\text{Eu}_4(\text{H}_2\text{O})_8\text{W}_6(\text{H}_6\text{glu})_4\text{O}_{12}(\text{B-}\alpha\text{-TeW}_9\text{O}_{33})_4]\}^{8-}$ POA fragment and the strongest peak centered at 1734.27 with a -7 charge state belongs to the $\{\text{Na}[\text{Eu}_4(\text{H}_2\text{O})_{10}\text{W}_6(\text{H}_6\text{glu})_4\text{O}_{12}(\text{B-}\alpha\text{-TeW}_9\text{O}_{33})_4]\}^{7-}$ POA fragment. It should be mentioned that the two low-intensity peaks at $m/z = 2017.87$ and 2040.50 are assigned to the $\{\text{K}_2[\text{Eu}_4(\text{H}_2\text{O})_4\text{W}_6(\text{H}_6\text{glu})_4\text{O}_{12}(\text{B-}\alpha\text{-TeW}_9\text{O}_{33})_4]\}^{6-}$ and $\{\text{K}_2[\text{Eu}_4(\text{H}_2\text{O})_{12}\text{W}_6(\text{H}_6\text{glu})_4\text{O}_{12}(\text{B-}\alpha\text{-TeW}_9\text{O}_{33})_4]\}^{6-}$ POA fragments. The peak at $m/z = 2460.27$ can be attributed to the $\{\text{K}_2\text{Na}[\text{Eu}_4(\text{H}_2\text{O})_{14}\text{W}_6(\text{H}_6\text{glu})_4\text{O}_{12}(\text{B-}\alpha\text{-TeW}_9\text{O}_{33})_4]\}^{5-}$ POA fragment. The occurrence of the above five characteristic m/z peaks is proof that the POA skeleton structure of **1** can be retained in water in the pH range of 2.01–9.97, although a small number of samples of **1** may be decomposed and re-

established in water. It is unusual to utilize several methods to test the stability of a POM in solution.

In addition, the stability of the POA skeleton structure of **1** in aqueous solution with time was also investigated using FL emission spectroscopy, UV spectroscopy and ESI-MS techniques. Initially, the FL intensity of **1** somewhat decreases. As we know, the RE FL behavior is greatly quenched by O–H and N–H vibrations, where the slight decrease of the FL intensity can be explained by the exchange of water ligands on Eu^{3+} ions with water molecules in solution and the dissociation of a small proportion of **1** in aqueous solution.³¹ It can be seen from Fig. S15a† that the FL intensity of the solution of **1** somewhat decreases from 0 to 2 h on account of rapid water exchange and the dissociation and re-establishment of a small proportion of **1** when **1** was dissolved in water. Afterwards, the FL intensity gradually recovered to the original intensity up to 8 h and remained unchanged upon an increase in time, which may be related to the exchange equilibrium established between the water ligands on the Eu^{3+} ions with the water molecules in aqueous solution and the dissociation of a proportion of **1** followed by re-establishment of a potentially new set of equilibria with the Eu^{3+} ions in the same type of coordination environments in aqueous solution. Furthermore, we also tested the FL behavior of $\text{Eu}(\text{NO}_3)_3 \cdot 6\text{H}_2\text{O}$ (Fig. S16b†). The emission peaks at 593, 614 and 701 nm can be assigned to the $^5\text{D}_0 \rightarrow ^7\text{F}_1$, $^5\text{D}_0 \rightarrow ^7\text{F}_2$ and $^5\text{D}_0 \rightarrow ^7\text{F}_4$ transitions of the Eu^{3+} ion. The FL emission behavior of the Eu^{3+} ion is highly sensitive to

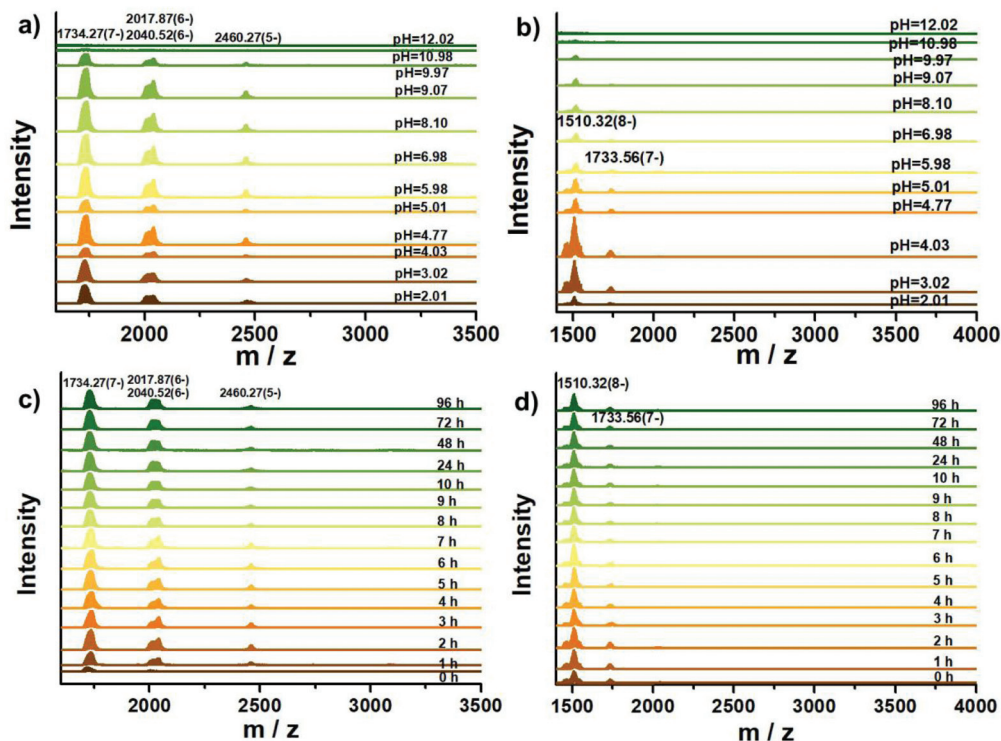


Fig. 7 (a) Enlarged view of the ESI-MS profiles in the range of 1600–3500 m/z of **1** in water at different pH values. (b) Evolution of the ESI-MS profiles of **1** in aqueous solution at different pH values. (c) Enlarged view of the ESI-MS profiles in the range of 1600–3500 m/z with time. (d) Evolution of the ESI-MS profiles of **1** with time in aqueous solution.

its local coordination environment.³² The magnetodipolar ${}^5D_0 \rightarrow {}^7F_2$ transition is inversely proportional to the site symmetry of the Eu^{3+} ion, where the ratio of $I({}^5D_0 \rightarrow {}^7F_2)/I({}^5D_0 \rightarrow {}^7F_1)$ always acts as a criterion by which to examine the coordination environment of the Eu^{3+} ion.³³ It is worth noting that the ratios of $I({}^5D_0 \rightarrow {}^7F_2)/I({}^5D_0 \rightarrow {}^7F_1)$ are 3.21 for **1** and 0.55 for $\text{Eu}(\text{NO}_3)_3 \cdot 6\text{H}_2\text{O}$, demonstrating that the Eu^{3+} ions in **1** are located in a low-symmetrical coordination environment while the Eu^{3+} ion in $\text{Eu}(\text{NO}_3)_3 \cdot 6\text{H}_2\text{O}$ inhabits a high-symmetrical coordination environment. Meanwhile, all the emission peaks of **1** simultaneously decreased over 2 h, and the ratio of $I({}^5D_0 \rightarrow {}^7F_2)/I({}^5D_0 \rightarrow {}^7F_1)$ remained almost unchanged upon an increase in the time (Table S3†). These results demonstrate that the coordination environments of the Eu^{3+} ions in **1** are unchanged in aqueous solution. Besides this, the decay lifetimes did not vary, which demonstrated that the coordination environments of the Eu^{3+} ions in **1** remained unchanged in aqueous solution as time went on (Fig. S17, Table S4†). The variable time UV spectra exhibit that two $\pi\pi$ - $d\pi$ charge-transfer absorption bands involving $\text{O}_t \rightarrow \text{W}$ and $\text{O}_{b(c)} \rightarrow \text{W}$ transitions show no conspicuous change over 96 h, supporting the fact that the POA skeleton structure of **1** does not decompose within 96 h (Fig. S16c†). The variable time stability of the POA skeleton structure of **1** in water was also investigated using ESI-MS. At 96 h, the m/z main peaks at 1510.32, 1733.56, 2017.87, 2040.52 and 2460.27 could be respectively assigned to molecular clusters with charges of -8 , -7 , -6 , -6 , -5 , as shown in Fig. 7c and d. The main peaks with m/z 1510.32 and 1733.56 can be unambiguously assigned to the $\{\text{Eu}_4(\text{H}_2\text{O})_8\text{W}_6(\text{H}_6\text{glu})_4\text{O}_{12}(\text{B-}\alpha\text{-TeW}_9\text{O}_{33})_4\}^{8-}$ and

$\{\text{Na}[\text{Eu}_4(\text{H}_2\text{O})_{10}\text{W}_6(\text{H}_6\text{glu})_4\text{O}_{12}(\text{B-}\alpha\text{-TeW}_9\text{O}_{33})_4]\}^{7-}$ POA species, the two peaks with m/z 2017.87 and 2040.52 can be attributed to $\{\text{K}_2[\text{Eu}_4(\text{H}_2\text{O})_4\text{W}_6(\text{H}_6\text{glu})_4\text{O}_{12}(\text{B-}\alpha\text{-TeW}_9\text{O}_{33})_4]\}^{6-}$ and the $\{\text{K}_2[\text{Eu}_4(\text{H}_2\text{O})_{12}\text{W}_6(\text{H}_6\text{glu})_4\text{O}_{12}(\text{B-}\alpha\text{-TeW}_9\text{O}_{33})_4]\}^{6-}$ POA fragments with two K^+ counter cations, and the observed peak with m/z 2460.27 can be ascribed to the $\{\text{K}_2\text{Na}[\text{Eu}_4(\text{H}_2\text{O})_{14}\text{W}_6(\text{H}_6\text{glu})_4\text{O}_{12}(\text{B-}\alpha\text{-TeW}_9\text{O}_{33})_4]\}^{5-}$ POA fragment. Similarly, the intensities and numbers of the m/z peaks remained almost unchanged in 96 h in contrast with the original ESI-MS spectrum, indicating that the POA skeleton structure of **1** is stable in aqueous solution, which prompted us to explore it as a luminescence sensor for metal ions.

Sensing of metal ions in aqueous solution

Up to now, the detection of metal ions in drinking water has drawn extensive attention because the excess metal ions cannot be degraded in the body and can cause various diseases. Although many optical materials have been utilized to detect metal ions, most of them have poor water solubility, which hinders their wide applications in the field of trace metal detection in aqueous systems. Herein, it can be seen that **1** not only shows good water solubility, but also excellent FL emission properties, which compelled us to explore it as a FL probe to detect trace metal ions in aqueous solution.

Among FL sensors, the variation in emission intensity with the detected object is a crucial factor for judging the capability of the sensing platform. Thus, 1.0 mL distilled water solutions containing 1.0 mg of **1** and 1.0 mM $\text{M}(\text{Cl})_x$ ($\text{M} = \text{Li}^+, \text{Na}^+, \text{K}^+, \text{Cs}^+, \text{Mg}^{2+}, \text{Ba}^{2+}, \text{Al}^{3+}, \text{Zn}^{2+}, \text{Cd}^{2+}, \text{Cu}^{2+}$) were respectively used in FL sensing experiments. As illustrated in Fig. 8a, in com-

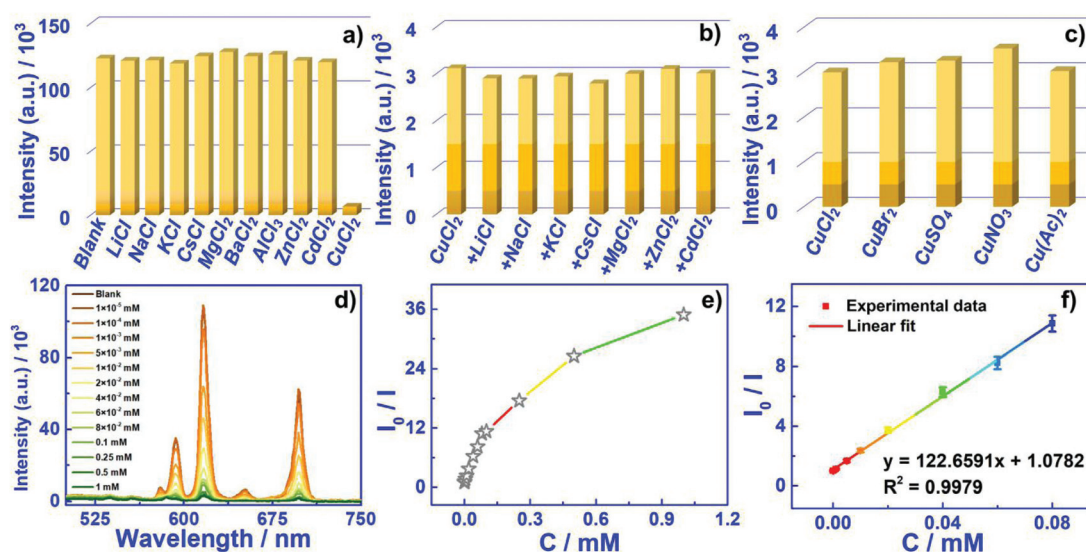


Fig. 8 (a) Variation in the FL emission at 614 nm of the **1**-sensor with the addition of different metal cations ($C_1 = 1.0 \text{ mg mL}^{-1}$, $\lambda_{\text{ex}} = 394 \text{ nm}$). (b) Variation in the FL emission at 614 nm of the **1**-sensor in the presence of 0.5 mM of Cu^{2+} cations and 0.5 mM of other heavy metal ions (the emission spectra were collected under excitation at 394 nm). (c) FL intensity at 614 nm of the sensor platform with the introduction of different Cu^{2+} salts. (d) Evolution of the emission spectra of the FL sensor in different Cu^{2+} concentrations. (e) Variation in the emission intensity at 614 nm at different Cu^{2+} concentrations (I_0 is the FL without Cu^{2+} cations, and I is the emission intensity under various conditions). (f) The linear variation of I/I_0 with the Cu^{2+} concentration in the range of 1.0×10^{-5} – 8.0×10^{-2} mM.

parison with that of a 1.0 mL distilled water solution containing only 1.0 mg of **1**, the emission intensity of the FL sensor **1** does not show any significant changes when the different solutions containing LiCl, KCl, NaCl, CsCl, MgCl₂, BaCl₂, AlCl₃, ZnCl₂ or CdCl₂, were measured by means of FL emission spectroscopy. This observation demonstrated that sensing **1** shows no obvious response toward alkali-metal ions (Li⁺, Na⁺, K⁺, Cs⁺), alkali-earth metal ions (Mg²⁺, Ba²⁺), main-group metal (Al³⁺) cations and transition-metal cations (Zn²⁺, Cd²⁺), indicating that sensing platform **1** cannot be used to detect these metal ions. However, a distilled water solution containing 1.0 mg of **1** and 1.0 mM of CuCl₂ was tested, and its emission intensity was apparently quenched, which manifests that sensing platform **1** shows a remarkable response toward Cu²⁺ ions (Fig. 8a, Fig. S18a†). Thus, sensing platform **1** can be employed to detect Cu²⁺ ions in aqueous solution. To our knowledge, although some POM-based FL sensors have been utilized to detect H₂O₂,³⁴ ascorbic acid,³⁵ and pH,³⁶ there have not been many investigations on the FL detection of Cu²⁺ ions using POM-based materials.^{37,38}

The selectivity of a FL sensor is also a significant factor, therefore, the anti-interference ability of sensor **1** for detecting Cu²⁺ ions was explored in solutions containing 0.5 mM of CuCl₂ and 0.5 mM of other metal ions (Fig. 8b, Fig. S18b†). The emission intensity of the FL probe **1** showed no obvious changes when Li⁺, Na⁺, K⁺, Cs⁺, Mg²⁺, Zn²⁺ or Cd²⁺ ions coexists were added to the Cu²⁺ ions in solution, suggesting that FL probe **1** has a high selectivity toward Cu²⁺ ions. Besides this, the influence of the anion on the FL sensor is also a crucial criterion to measure the selectivity of FL detection. Thus, the effects of different anions on the FL sensor of **1** were also examined (Fig. 8c, Fig. S18c†). The results indicated that the emission intensities of the FL sensor **1** were almost unchanged with the variation in different copper sources (CuSO₄, CuCl₂, CuBr₂, Cu(Ac)₂, CuNO₃. C = 1.0 mM). This outstanding anti-interference ability means that the FL sensor **1** is suitable for sensing Cu²⁺ ions in complex circumstances.

In addition, evaluating the sensitivity of a FL sensor is very important. Thus, to investigate the sensitivity of the FL sensor further, the emissive response of the FL platform for detecting Cu²⁺ ions was measured in the range from 1.0 × 10⁻⁵ to 1.0 mM. Fig. 8d shows that the emission intensity of **1** decreases on increasing the concentration of the Cu²⁺ ions. K_{SV} is the Stern–Volmer constant, which reflects the sensitivity of the sensing platform.³⁹ The K_{SV} value of the sensor was calculated as 123.17 mM⁻¹ when the concentration of the Cu²⁺ ions was 8.0 × 10⁻² mM, according to the Stern–Volmer eqn (1).

$$I_0/I = 1 + K_{SV}[Cu^{2+}] \quad (1)$$

wherein I₀ and I are the main emission peaks at 614 nm in the absence and presence of Cu²⁺ ions. Compared with some reported sensors that can be used to monitor Cu²⁺ ions, the sensor based on **1** shows a higher K_{SV} value, indicating that the sensor has favorable accuracy and precision for monitoring Cu²⁺ ions (Table S5†).⁴⁰ Besides this, the I₀/I versus [Cu²⁺] is

linearly dependent in the range of 1.0 × 10⁻⁵–8.0 × 10⁻² mM, and the regression equation is I₀/I = 122.6591[Cu²⁺] + 1.0782, giving a LOD value of 8.82 × 10⁻⁶ mM based on three times the standard deviation of the blank sample measurement (2) (Fig. 8e and f).⁴¹

$$LOD = 3s/k \quad (2)$$

The standard deviation (s) was calculated from three blank emission intensities of the sensor, where the slope (k) was found to be 122.6591, and the corresponding regression coefficient R² was 0.9979 (Tables S6 and S7†). It is promising that the LOD of this sensor is far lower than the maximum concentration of the Cu²⁺ ions that normal healthy cells can withstand (0.1 mM) and the WHO required levels of Cu²⁺ ions in the daily use of water.⁴¹ Currently, a survey of sensors for detecting Cu²⁺ ions shows that the sensors are mainly anthracene, pyrene, quinoline, quinazoline, dansyl, naphthalimide organic derivatives, quantum dots and 3D metal–organic frameworks (MOFs).⁴² Some polypeptide-, protein- and DNA-based FL sensors have also been investigated to detect trace Cu²⁺ ions (Fig. 9).⁴³ To evaluate the sensing performance of the RECTT-based FL towards Cu²⁺ ions, we compared the LOD value with the values in the literature. As shown in Table 1, the novel **1**-based FL sensor exhibits better analytical performance for detecting Cu²⁺ ions.^{44–47} This result might be due to the excellent water solubility and stable FL characteristics of **1**.

Studies on the quenching mechanism of Cu²⁺ ions

Many mechanisms can be used to detect the concentration of Cu²⁺ ions, such as chelation between Cu²⁺ ions and N atoms on the sensor, the deprotonation of N–H in presence of Cu²⁺ ions, dynamic collision between Cu²⁺ ions and the sensor, molecular rearrangement, energy or electron transfer between the sensor and Cu²⁺ ions.⁴⁸ To investigate the operational

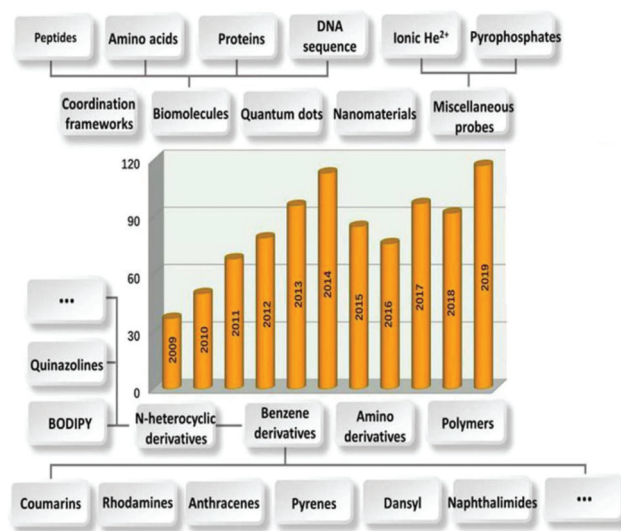


Fig. 9 A histogram of some FL sensors for detecting Cu²⁺ ions that were reported between 2009 and 2019.

Table 1 Comparison of the sensitivities of different sensor probes for detecting Cu²⁺ ions

FL modes	FL reagents	Linear range (mM)	LOD (mM)	Testing media	Ref.
Turn-off ($\lambda_{\text{ex}} = 350$ nm)	Silicon nanowires	0.5×10^{-4} to 4.0×10^{-3}	3.1×10^{-5}	10 mM HEPES buffer (pH = 7.4)	41b
Turn-on-off ($\lambda_{\text{ex}} = 246$ nm)	Multiple benzene and pyridine derivatives	0 to 2.0×10^{-2}	5.0×10^{-3}	Ethanol solution	2b
Turn-off ($\lambda_{\text{ex}} = 345$ nm)	Bis-pyrene derivative	1.0×10^{-3} to 1.5×10^{-2}	5.0×10^{-5}	10 mM Tris-HCl buffer solution (pH = 7.4)	15
Turn-off ($\lambda_{\text{ex}} = 290$ nm)	Ce(III) coordination supramolecular compound	5.0×10^{-3} to 0.1	3×10^{-3}	Water	39a
Turn-on ($\lambda_{\text{ex}} = 360$ nm)	Diarylethene moiety	0 to 3.0×10^{-2}	9.1×10^{-5}	CH ₃ CN	44
Turn-on ($\lambda_{\text{ex}} = 480$ nm)	DNA-Ag nanoparticles	1.0×10^{-5} to 2.0×10^{-4}	8.0×10^{-6}	Water	45
Turn-off ($\lambda_{\text{ex}} = 400$ nm)	Carbon quantum dots (CQDs)	1.0×10^{-3} to 1	1.0×10^{-3}	10 mM phosphate buffered saline (PBS) solution	46
Turn-off ($\lambda_{\text{ex}} = 340$ nm)	covalently connecting between CdTe quantum dots (QDs) and CQDs	0 to 3.0×10^{-4}	3.6×10^{-4}	Water	47
Turn-off ($\lambda_{\text{ex}} = 394$ nm)	Eu-containing TTs	1×10^{-5} to 8×10^{-2}	8.82×10^{-6}	Water	Our work

mechanism of the sensor platform for metal ions, numerous experiments were carried out.

Initially, in order to probe the FL quenching mechanism of the **1**-sensor toward Cu²⁺, a solution containing Cu²⁺ and **1** was studied using ESI-MS, to investigate whether a new compound is formed during the detection of Cu²⁺ using **1**. The ESI-MS results exhibit that the *m/z* peaks are consistent with those of a solution of **1** and no new *m/z* peak resulting from a complex assembled from Cu²⁺ and **1a** is observed, demonstrating that there is no obvious bonding interaction that occurs between Cu²⁺ and **1a** (Fig. S19†). Furthermore, to intuitively prove that there are no new generated compounds in the process of detecting Cu²⁺, we tried to grow crystals of **1** from a solution containing 100 mM of Cu²⁺. What is exciting is that colorless crystals of **1** could still be grown from the solution containing 100 mM of Cu²⁺ and the IR spectrum and XRD pattern of the crystals of **1** grown from the solution containing Cu²⁺ are consistent with those of **1** (Fig. S20†), which indicates that there is no coordination effect that occurs between Cu²⁺ and **1a**. X-ray photoelectron spectroscopy (XPS) experiments were utilized to explore the affinity between Cu²⁺ ions and sensor **1**. Comparing the XPS spectrum of pure crystals of **1** with that of the crystals grown from the solution containing Cu²⁺ ions, the binding energies of the O, W, Eu Te and C elements show no blue or red shifts. Thus, there are no interactions between the Cu²⁺ cations and sensor **1** (Fig. S21†). Furthermore, the temperature-dependent luminescence emission spectra of **1** in solutions containing 0.001 mM of Cu²⁺ ions were recorded in the range of 20–90 °C (Fig. S22a†). If the quenching mechanism is a result of dynamic collision between the Cu²⁺ ions and sensor **1**, the collision would become more vigorous upon an increase in temperature, leading to a thermal quenching effect. Compared with the temperature-dependent emission spectra of **1** in solution in the absence of Cu²⁺ ions (Fig. S22b†), the slight decrease in the emission intensity of the solution containing both **1** and Cu²⁺ can be attributed to the increased O–H and N–H vibrations upon an increase in temperature.²⁹ After adding

Cu²⁺ ions to the sensor, the inconspicuous quenching effect proves that the detection mechanism does not follow a dynamic quenching mechanism. Thus, the FL quenching effect may be caused by the nature of Cu²⁺ in the aqueous solution. Therefore, to determine the quenching mechanism, UV-vis spectra of the solutions of 1.0 mM Cu²⁺, Li⁺, Na⁺, K⁺, Cs⁺, Mg²⁺, Ba²⁺, Al³⁺, Zn²⁺ or Cd²⁺ were recorded, in which an obvious absorption band for the Cu²⁺ solution was observed between 190 and 237 nm, while no absorption band from 190 to 400 nm was observed for the Li⁺, Na⁺, K⁺, Cs⁺, Mg²⁺, Ba²⁺, Al³⁺, Zn²⁺ or Cd²⁺ solutions (Fig. 10). Thus, the emission quenching effect may be related to the fact the mechanism and contribution of the non-radiative relaxation in the presence of Cu²⁺ ions has changed, which leads to the FL quenching of sensor **1**.^{44,49}

Detection of Cys

Moreover, developing reversible response smart materials has captured considerable attention on account of their various applications in molecular electronics, nanotechnology and bio-devices.⁵⁰ If FL properties of the Cu²⁺-quenching system of sensor **1** under some external stimulus conditions can be gradually recovered, this Cu²⁺-quenching system will realize an “off-on” switching effect. Amino acids are indispensable for

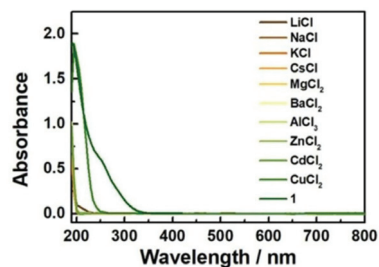


Fig. 10 UV-vis spectra of 1.0 mM of different metal ions in aqueous solution.

the survival of humans and animals and have a strong bonding affinity for transition metal ions.⁵¹ Therefore, the fabrication of a self-regenerating “off-on” sensor based on **1** to detect amino acids has attracted keen interest.

To explore the sensing selectivity of the Cu²⁺-quenching system toward different amino acids, FL emission measurements of the Cu²⁺-quenching system were performed in the presence of Cys, glycine (Gly), threonine (Thr), glutamic acid (Glu), and lysine (Lys), respectively. As shown in Fig. 11a and Fig. S23,[†] the FL emission of the Cu²⁺-quenching system can be effectively recovered upon the addition of Cys. ESI-MS spectra exhibit that the skeleton of **1** does not change with the addition of Cu²⁺ and Cys (Fig. S24[†]). The “off-on” switching of the Cu²⁺-quenching system is caused by the strong chelation between Cys and Cu²⁺.⁵² In order to evaluate the sensitivity of the “off-on” sensor toward the detection of Cys, the emission intensity of the Cu²⁺-quenching sensor was gradually recovered by increasing the concentration of Cys to within the range of 0.02–0.20 mM (Fig. 11b and c). The linear relationship between 0.02 and 0.14 mM gave a LOD of 1.75×10^{-4} mM, which was calculated from $\text{LOD} = 3s/k$, where the value of k was determined as 33.8079 from the fitted linear equation: $y = 33.8079x + 0.3778$ (Fig. 11d, Table S8 and S9[†]). These results suggest that the unique structure of **1** can be used as a highly effective “off-on” sensor for detecting Cys. Besides this, the FL recovery efficiency (R_E) of Cys was calculated according to the equation $R_E = I/I_0 - 1$ (I and I_0 are the emission intensities of the FL sensor in the presence and absence of Cys, respectively).⁵³ The relative R_E is 4.07 when the concentration of Cys

is the highest (0.14 mM) in the linear range, indicating a benign recovery efficiency of the “off-on” sensor. At the same time, it can be clearly seen that the excitation intensities of the Cu²⁺-quenching system under the emission band of 614 nm

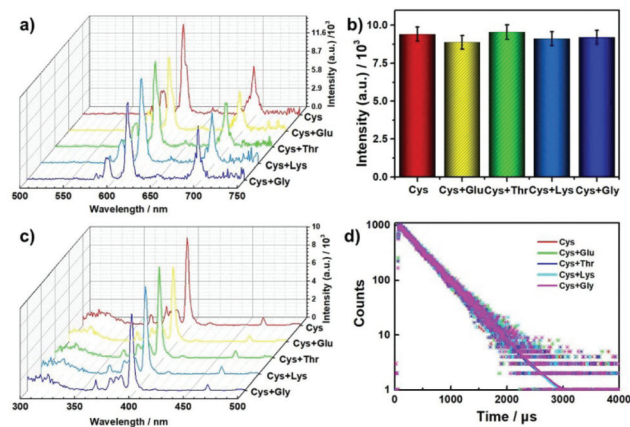


Fig. 12 (a) Changes in the emission spectra of the Cu²⁺-quenching system based on **1** (0.04 mM Cu²⁺ cation) in the presence of both 0.10 mM of Cys and 0.10 mM of other amino acids. (b) Changes in the FL emission at 614 nm of the Cu²⁺-quenching system (0.04 mM of Cu²⁺ ions) in the presence of both 0.10 mM of Cys and 0.10 mM of other amino acids. (c) Changes in the excitation spectra of the Cu²⁺-quenching system (0.04 mM of Cu²⁺ ions) in the presence of both 0.10 mM of Cys and 0.10 mM of other amino acids. (d) Changes in the lifetime decay curves of the Cu²⁺-quenching system (0.04 mM of Cu²⁺ ions) in the presence of both 0.10 mM of Cys and 0.10 mM of other amino acids.

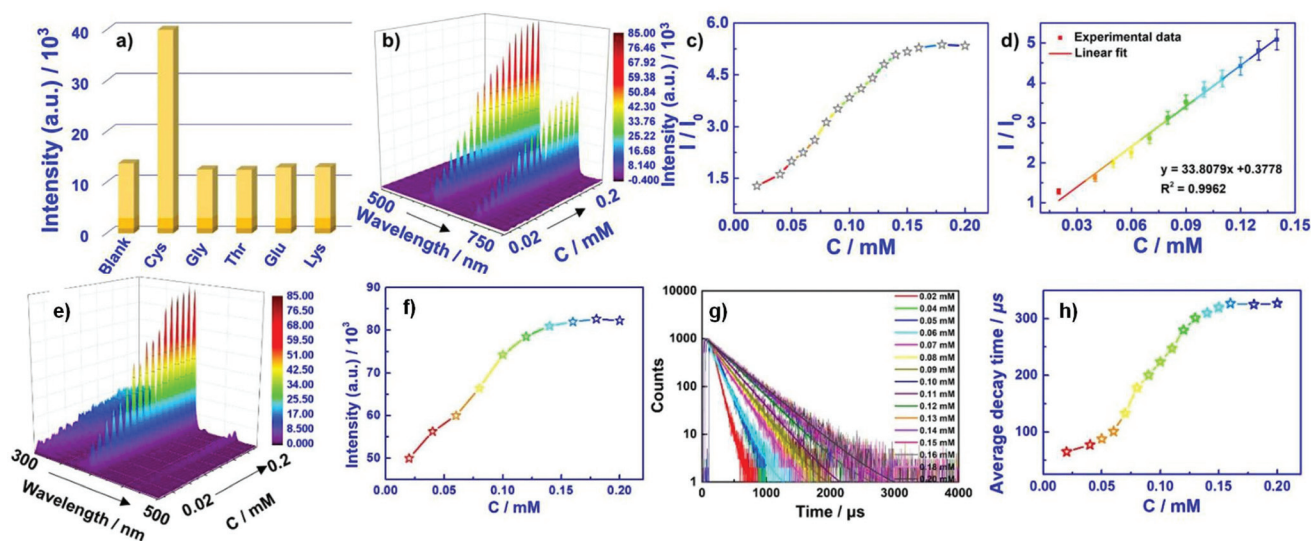


Fig. 11 (a) Change of the emission intensity at 614 nm of the Cu²⁺-quenching system based on **1** with addition of diverse aminoacids ($C_1 = 1.0$ mg mL⁻¹, $\lambda_{\text{ex}} = 394$ nm). (b) Evolution of emission spectra of the Cu²⁺-quenching system based on **1** in different concentrations of Cys. (c) Variation of I/I_0 value of the emission intensity at 614 nm of the Cu²⁺-quenching system based on **1** with the concentration of Cys ($C_{\text{Cu}^{2+}} = 4.00 \times 10^{-2}$ mM) (I is the emission intensity at 614 nm in different concentrations of Cys and I_0 is the emission intensity at 614 nm in the absence of Cys). (d) The linear variation of I/I_0 with the concentration of Cys ($C_{\text{Cu}^{2+}} = 4.00 \times 10^{-2}$ mM). (e) Evolution of excitation spectra of the Cu²⁺-quenching system based on **1** in different concentrations of Cys. (f) Change of the excitation intensity at 394 nm of the Cu²⁺-quenching system based on **1** in different concentrations of Cys. (g) Lifetime decay curves of the Cu²⁺-quenching system based on **1** in different concentrations of Cys. (h) Change of the average decay time (τ^*) in different concentrations of Cys.

gradually increase upon increasing the concentration of Cys (Fig. 11e). The tendency of the excitation bands to recover is highly consistent with the trend of the emission bands, suggesting that the Cu²⁺-quenching system efficiently detects Cys (Fig. 11f). Besides this, the decay lifetimes of the Cu²⁺-quenching system generally increased upon an increase in the concentration of Cys, and the unique “smart switch” effect of the Cu²⁺-quenching system prompted us to investigate more potential applications of POM frameworks (Fig. 11g and h). The emission remained unchanged with the addition of Gly, Thr, Glu and Lys, respectively, probably due to the lack of sulfhydryl groups in Gly, Thr, Glu and Lys. The above phenomena exhibit that the Cu²⁺-quenching system could be used as an effective “off-on” sensor toward the detection of Cys by recovering the FL intensity of the Cu²⁺-quenching system through the strong chelation between Cys and Cu²⁺.

Furthermore, the anti-interference capability of the sensor was also measured *via* the coexistence of 0.10 mM of Cys and 0.10 mM other amino acids in the detection system (Fig. 12a and b). The recovered FL intensities of the emission peaks were found to not be affected by the addition of Glu, Thr, Lys, or Gly, respectively. The excitation bands and decay lifetimes of the Cu²⁺-quenching system showed no obvious fluctuations when the detection system simultaneously contained Cys and other amino acids, proving that it has high selectivity for detecting Cys (Fig. 12c and d).

Conclusions

In summary, the first unprecedented gluconic acid bridged multi-Eu^{III}-incorporated TT **1** was resoundingly isolated *via* an organic-ligand-driven self-assembly strategy. Appreciably, the four flexible H₆glu ligands can be viewed as adhesives that induce the aggregation of four trilacunary TT subunits and Eu³⁺ ions. As far as we know, it is uncommon for a polyhydroxycarboxylic acid ligand to adopt such a five-coordinate mode in the construction of POMs. The FL sensor **1** exhibits high FL activity and good selectivity for detecting Cu²⁺ ions in aqueous solution with a LOD of 8.82×10^{-6} mM, making it the most sensitive POM-based FL sensor for detecting Cu²⁺ ions in aqueous solution. Furthermore, a Cu²⁺-quenching system of **1** was used to construct an “off-on” FL sensor to detect Cys in aqueous solution with a LOD of 1.75×10^{-4} mM. The innovative exploration of **1** as a combined “on-off” Cu²⁺ monitoring “off-on” Cys detecting sensor provides a feasible avenue for synthesizing POM-based materials as “smart materials” to be used in the fields of environmental water treatment, medical testing and food industry monitoring.

Conflicts of interest

There are no conflicts to declare.

Acknowledgements

This work was supported by the National Natural Science Foundation of China (21671054, 21571048, 21771052, 21871077), the Program for Innovation Teams in Science and Technology in Universities of Henan Province (20IRTSTHN004), the Program of First-Class Discipline Cultivation Project of Henan University (2019YLZDYJ02) and the Postgraduate Education Innovation and Quality Improvement Plan of Henan University (SYL18060130).

Notes and references

- (a) S. Craig, *Science*, 2019, **363**, 451; (b) M. J. Serpe, *Nature*, 2019, **565**, 438; (c) N. P. Lu, P. F. Zhang, Q. H. Zhang, R. M. Qiao, Q. He, H.-B. Li, Y. J. Wang, J. W. Guo, D. Zhang, Z. Duan, Z. L. Li, M. Wang, S. Z. Yang, M. Z. Yan, E. Arenholz, S. Y. Zhou, W. L. Yang, L. Gu, C.-W. Nan, J. Wu, Y. Tokura and P. Yu, *Nature*, 2017, **546**, 124; (d) B. A. Korgel, *Nature*, 2013, **500**, 278; (e) X.-Y. Dong, B. Li, B.-B. Ma, S.-J. Li, M.-M. Dong, Y.-Y. Zhu, S.-Q. Zang, Y. Song, H.-W. Hou and T. C. W. Mak, *J. Am. Chem. Soc.*, 2013, **135**, 10214.
- (a) D. Kraskouskaya, M. Bancercz, H. S. Soor, J. E. Gardiner and P. T. Gunning, *J. Am. Chem. Soc.*, 2014, **136**, 1234; (b) Z. X. Li, L. F. Zhang, L. N. Wang, Y. K. Guo, L. H. Cai, M. M. Yu and L. H. Wei, *Chem. Commun.*, 2011, **47**, 5798; (c) M. Lu, J. Liu, Q. Li, M. Zhang, M. Liu, J.-L. Wang, D.-Q. Yuan and Y.-Q. Lan, *Angew. Chem., Int. Ed.*, 2019, **58**, 12392; (d) Z. Wang, F. Su, C. H. Tung, D. Sun and L. S. Zheng, *Nat. Commun.*, 2018, **9**, 4407; (e) S. Li, X.-S. Du, B. Li, J.-Y. Wang, G.-P. Li, G.-G. Gao and S.-Q. Zang, *J. Am. Chem. Soc.*, 2018, **140**, 594.
- (a) J. A. Mattocks, J. V. Ho and J. A. Cotruvo, *J. Am. Chem. Soc.*, 2019, **141**, 2857; (b) Z. L. Yang, K. Y. Loh, Y.-T. Chu, R. Feng, N. S. R. Satyavolu, M. Y. Xiong, S. M. N. Huynh, K. Hwang, L. L. Li, H. Xing, X. B. Zhang, Y. R. Chemla, M. Gruebels and Y. Lu, *J. Am. Chem. Soc.*, 2018, **140**, 17656.
- (a) Y.-J. Wang, S.-Y. Wu, Y.-Q. Sun, X.-X. Li and S.-T. Zheng, *Chem. Commun.*, 2019, **55**, 2857; (b) J.-C. Liu, Q. Han, L.-J. Chen, J.-W. Zhao, C. Streb and Y.-F. Song, *Angew. Chem., Int. Ed.*, 2018, **57**, 8416; (c) J. C. Liu, J. Luo, Q. Han, J. Cao, L. J. Chen, Y. Song and J. W. Zhao, *J. Mater. Chem. C*, 2017, **5**, 2043; (d) C. Boskovic, *Acc. Chem. Res.*, 2017, **50**, 2205; (e) Z. Li, X.-X. Li, T. Yang, Z.-W. Cai and S.-T. Zheng, *Angew. Chem., Int. Ed.*, 2017, **56**, 2664; (f) Y.-L. Wu, X.-X. Li, Y.-J. Qi, H. Yu, L. Jin and S.-T. Zheng, *Angew. Chem., Int. Ed.*, 2018, **57**, 1; (g) S. Reinoso, M. Giménez-Marqués, J. R. Galán-Mascarós, P. Vitoria and J. M. Gutiérrez-Zorrilla, *Angew. Chem., Int. Ed.*, 2010, **49**, 8384; (h) B. S. Bassil, M. H. Dickman, I. Römer, B. von der Kammer and U. Kortz, *Angew. Chem., Int. Ed.*, 2007, **46**, 6192; (i) J. Jiang, J. R. Duan, J. C. Liu, L. J. Chen and J. W. Zhao, *Cryst. Growth Des.*, 2020, **20**, 362; (j) N. Li, J. Liu, J.-J. Liu, L.-Z. Dong, S.-L. Li, B.-X. Dong, Y.-H. Kan and Y.-Q. Lan,

- Angew. Chem., Int. Ed.*, 2019, **58**, 17260; (k) Y. Yang, T. Jia, Y.-Z. Han, Z.-A. Nan, S.-F. Yuan, F.-L. Yang and D. Sun, *Angew. Chem., Int. Ed.*, 2019, **58**, 12280.
- 5 (a) T. Yamase, *Chem. Rev.*, 1998, **98**, 307; (b) Y. Li, H. Li, J. Jiang, L. Chen and J. Zhao, *Inorg. Chem.*, 2019, **58**, 3479; (c) C. Zhang, R. C. Howell, D. McGregor, L. Bensaid, S. Rahyab, M. Nayshtut, S. Lekperic and L. C. Francesconi, *C. R. Chim.*, 2005, **8**, 1035; (d) C. M. Prosser-McCartha, M. Kadkhodayan, M. M. Williamson and C. L. Hill, *J. Chem. Soc., Chem. Commun.*, 1986, 1747.
- 6 (a) W.-C. Chen, H.-L. Li, X.-L. Wang, K.-Z. Shao, Z.-M. Su and E.-B. Wang, *Chem. – Eur. J.*, 2013, **19**, 11007; (b) C. H. Zhan, J. M. Cameron, J. Gao, J. W. Purcell, D. L. Long and L. Cronin, *Angew. Chem., Int. Ed.*, 2014, **53**, 10362.
- 7 Q. Han, Y. Wen, J.-C. Liu, W. Zhang, L.-J. Chen and J.-W. Zhao, *Inorg. Chem.*, 2017, **56**, 13228.
- 8 Q. Han, J.-C. Liu, Y. Wen, L.-J. Chen, J.-W. Zhao and G.-Y. Yang, *Inorg. Chem.*, 2017, **56**, 7257.
- 9 J.-C. Liu, J.-W. Zhao and Y.-F. Song, *Inorg. Chem.*, 2019, **58**, 9706.
- 10 (a) Q. Zheng, L. Vilà-Nadal, Z. L. Lang, J.-J. Chen, D.-L. Long, J. S. Mathieson, J. M. Poblet and L. Cronin, *J. Am. Chem. Soc.*, 2018, **140**, 2595; (b) K. Wassermann, M. H. Dickman and M. T. Pope, *Angew. Chem., Int. Ed. Engl.*, 1997, **36**, 1445; (c) K. Fukaya and T. Yamase, *Angew. Chem., Int. Ed.*, 2003, **42**, 654; (d) H.-L. Li, Y.-J. Liu, Y.-M. Li, L.-J. Chen, J.-W. Zhao and G.-Y. Yang, *Chem. – Asian J.*, 2018, **13**, 2897; (e) H.-L. Li, C. Lian, L.-J. Chen, J.-W. Zhao and G.-Y. Yang, *Inorg. Chem.*, 2019, **58**, 8442.
- 11 J. Gao, J. Yan, S. Beeg, D.-L. Long and L. Cronin, *Angew. Chem., Int. Ed.*, 2012, **51**, 3373.
- 12 C. Ritchie, V. Baslon, E. G. Moore, C. Reber and C. Boskovic, *Inorg. Chem.*, 2012, **51**, 1142.
- 13 J.-W. Zhao, Y.-Z. Li, L.-J. Chen and G.-Y. Yang, *Chem. Commun.*, 2016, **52**, 4418.
- 14 A. Dolbecq, E. Dumas, C. R. Mayer and P. Mialane, *Chem. Rev.*, 2010, **110**, 6009.
- 15 L. P. Ding, S. H. Wang, Y. Liu, J. H. Cao and Y. Fang, *J. Mater. Chem. A*, 2013, **1**, 8866.
- 16 G. M. Sheldrick, *SADABS*, University of Göttingen, Göttingen, Germany, 2016.
- 17 (a) G. M. Sheldrick, *Acta Crystallogr., Sect. C: Struct. Chem.*, 2015, **71**, 3; (b) L. J. Bourhis, O. V. Dolomanov, R. J. Gildea, J. A. K. Howard and H. Puschmann, *Acta Crystallogr., Sect. A: Found. Adv.*, 2015, **71**, 59; (c) O. V. Dolomanov, L. J. Bourhis, R. J. Gildea, J. A. K. Howard and H. Puschmann, *J. Appl. Crystallogr.*, 2009, **42**, 339.
- 18 S. X. Shang, Z. G. Lin, A. X. Yin, S. Yang, Y. N. Chi, Y. Wang, J. Dong, B. Liu, N. Zhen, C. L. Hill and C. W. Hu, *Inorg. Chem.*, 2018, **57**, 8831.
- 19 (a) J. Gao, J. Yan, S. G. Mitchell, H. N. Miras, A. G. Boulay, D.-L. Long and L. Cronin, *Chem. Sci.*, 2011, **2**, 1502; (b) Q. Zhen, L. Vilà-Nadal, Z. L. Lang, J.-J. Chen, D.-L. Long, J. S. Mathieson, J. M. Poblet and L. Cronin, *J. Am. Chem. Soc.*, 2018, **140**, 2595.
- 20 D. M. Zheng, R. Q. Wang, Y. Du, G. F. Hou, L. X. Wu and L. H. Bi, *New J. Chem.*, 2016, **40**, 8829.
- 21 H. Y. An, Z. B. Han and T. Q. Xu, *Inorg. Chem.*, 2010, **49**, 11403.
- 22 G. B. Deacon and R. J. Phillips, *Coord. Chem. Rev.*, 1980, **33**, 227.
- 23 D. Y. Shi, J. W. Zhao, L. J. Chen, P. T. Ma, J. P. Wang and J. Y. Niu, *CrystEngComm*, 2012, **14**, 3108.
- 24 (a) E. Álvarez, M. E. Zayas, J. Alvarado-Rivera, F. Félix-Domínguez, R. P. Duarte-Zamorano and U. Caldiño, *J. Lumin.*, 2014, **153**, 198; (b) H.-L. Li, Y.-J. Liu, J.-L. Liu, L.-J. Chen, J.-W. Zhao and G.-Y. Yang, *Chem. – Eur. J.*, 2017, **23**, 2673; (c) X. Xu, H. Li, S. S. Xie, L. Mei, R. R. Meng, L. J. Chen and J. W. Zhao, *Inorg. Chem.*, 2020, **59**, 648.
- 25 (a) M. Sugeta and T. Yamase, *Bull. Chem. Soc. Jpn.*, 1993, **66**, 444; (b) T. Yamase, H. Naruke and Y. J. Sasaki, *J. Chem. Soc., Dalton Trans.*, 1990, 1687; (c) T. Yamase, T. Kobayashi and S. F. A. Kettle, *J. Electrochem. Soc.*, 1996, **143**, 1678; (d) T. Ozeki and T. Yamase, *J. Alloys Compd.*, 1993, **192**, 28; (e) M. M. Williamson, D. A. Bouchard and C. L. Hill, *Inorg. Chem.*, 1987, **26**, 1436; (f) T. Yamase, T. Kobayashi, M. Sugeta and H. Naruke, *J. Phys. Chem. A*, 1997, **101**, 5046; (g) J. Jing, B. P. Burton-Pye, L. C. Francesconi and M. R. Antonio, *Inorg. Chem.*, 2008, **47**, 6889; (h) C. Ritchie, E. G. Moore, M. Speldrich, P. Kögerler and C. Boskovic, *Angew. Chem., Int. Ed.*, 2010, **49**, 7702.
- 26 Y. J. Cui, Y. F. Yue, G. D. Qian and B. L. Chen, *Chem. Rev.*, 2012, **112**, 1126.
- 27 C. Ritchie, K. G. Alley and C. Boskovic, *Dalton Trans.*, 2010, **39**, 8872.
- 28 (a) H. Y. Zang, H. N. Miras, J. Yan, D.-L. Long and L. Cronin, *J. Am. Chem. Soc.*, 2012, **134**, 11376; (b) S. Z. Li, J. W. Zhao, P. T. Ma, J. Du, J. Y. Niu and J. P. Wang, *Inorg. Chem.*, 2009, **48**, 9819.
- 29 (a) J.-W. Zhao, H.-L. Li, X. Ma, Z. G. Xie, L.-J. Chen and Y. S. Zhu, *Sci. Rep.*, 2016, **6**, 26406; (b) C. C. Zhao, C. S. Kambara, Y. Yang, A. L. Kaledin, D. G. Musaev, T. Q. Lian and C. L. Hill, *Inorg. Chem.*, 2013, **52**(2), 671.
- 30 (a) J. Gao, J. Yan, S. Beeg, D.-L. Long and L. Cronin, *J. Am. Chem. Soc.*, 2013, **135**, 1796; (b) D.-L. Long, C. Streb, Y.-F. Song, S. Mitchell and L. Cronin, *J. Am. Chem. Soc.*, 2008, **130**, 1830; (c) E. F. Wilson, H. Abbas, B. J. Duncombe, C. Streb, D.-L. Long and L. Cronin, *J. Am. Chem. Soc.*, 2008, **130**, 13876; (d) E. F. Wilson, H. N. Miras, M. H. Rosnes and L. Cronin, *Angew. Chem., Int. Ed.*, 2011, **50**, 3720; (e) P. J. Robbins, A. J. Surman, J. Thiel, D.-L. Long and L. Cronin, *Chem. Commun.*, 2013, **49**, 1909; (f) C. Dablemont, A. Proust, R. Thouvenot, C. Afonso, F. Fournier and J.-C. Tabet, *Inorg. Chem.*, 2004, **43**, 3514; (g) J. M. Cameron, L. Vilà-Nadal, R. S. Winter, F. Iijima, J. C. Murillo, A. Rodríguez-Forteza, H. Oshio, J. M. Poblet and L. Cronin, *J. Am. Chem. Soc.*, 2016, **138**, 8765.
- 31 (a) S. Quici, M. Cavazzini, G. Marzanni, G. Accorsi, N. Armaroli, B. Ventura and F. Barigelletti, *Inorg. Chem.*, 2005, **44**, 529; (b) K. Y. Wang, B. S. Bassil, Z. G. Lin, I. Römer, S. Vanhaecht, T. N. Parac-Vogt, C. S. de Pipaún,

- J. R. Galan-Mascarós, L. Y. Fan, J. Cao and U. Kortz, *Chem. – Eur. J.*, 2015, **21**, 18168; (c) G. Hungerford, F. Hussain, G. R. Patzke and M. Green, *Phys. Chem. Chem. Phys.*, 2010, **12**, 7266.
- 32 D. L. R. Reisfeld and D. Avnir, *Chem. Phys. Lett.*, 1984, **109**, 593.
- 33 K. Binnemans, *Chem. Rev.*, 2009, **109**, 4283.
- 34 J. Lu, Q. Kang, J. H. Xiao, T. Wang, M. Fang and L. Yu, *Carbohydr. Polym.*, 2018, **200**, 560.
- 35 Z. J. Fu, W. M. Gao, T. Yu and L. H. Bi, *Talanta*, 2019, **195**, 463.
- 36 (a) A. M. Kaczmarek, *J. Mater. Chem. C*, 2018, **6**, 5916; (b) J. Yang, M. Chen, P. Li, F. Cheng, Y. Xu, Z. Q. Li, Y. G. Wang and H. R. Li, *Sens. Actuators, B*, 2018, **273**, 153.
- 37 C. X. Xia, S. S. Zhang, Y. B. Tan, D. Sun, P. P. Sun, X. H. Cheng and X. Xin, *ACS Omega*, 2018, **3**, 14953.
- 38 (a) T. Dutta and S. Sarkar, *Appl. Nanosci.*, 2016, **6**, 1191; (b) Y. X. Guo, Y. J. Gong, L. B. Qi, Y. A. Gao and L. Yu, *J. Colloid Interface Sci.*, 2017, **485**, 280; (c) H. Liu, Y. Lv, S. Li, F. Yang, S. Liu, C. Wang, J.-Q. Sun, H. Meng and G.-G. Gao, *J. Mater. Chem. C*, 2017, **5**, 9383.
- 39 (a) S. Geranmayeh, M. Mohammadnejad and S. Mohammadi, *Ultrason. Sonochem.*, 2018, **40**, 453; (b) Z. F. Wu and X. Y. Huang, *ChemistrySelect*, 2018, **3**, 4884.
- 40 (a) P. Samanta, A. V. Desai, S. Sharma, P. Chandra and S. K. Ghosh, *Inorg. Chem.*, 2018, **57**, 2360; (b) P. Zhang, J. Jiang, R. Yuan, Y. Zhuo and Y. Q. Chai, *J. Am. Chem. Soc.*, 2018, **140**, 9361.
- 41 (a) J. X. Yin, X. Ma, G. H. Wei, D. B. Wei and Y. G. Du, *Sens. Actuators, B*, 2013, **177**, 213; (b) R. Miao, L. X. Mu, H. Y. Zhang, G. W. She, B. J. Zhou, H. T. Xu, P. F. Wang and W. S. Shi, *Nano Lett.*, 2014, **14**, 3124.
- 42 G. Sivaraman, M. Iniya, T. Anand, N. G. Kotla, O. Sunnapu, S. Singaravavel, A. Gulyani and D. Chellappa, *Coord. Chem. Rev.*, 2018, **357**, 50.
- 43 (a) R. H. Jung, E.-T. Oh, H. J. Park and K.-H. Lee, *Biosens. Bioelectron.*, 2016, **85**, 437; (b) J.-L. He, S.-L. Zhu, P. Wu, P.-P. Li, T. Li and Z. Cao, *Biosens. Bioelectron.*, 2014, **60**, 112; (c) P.-P. Hu, N. Liu, K.-Y. Wu, L.-Y. Zhai, B.-P. Xie, B. Sun, W.-J. Duan and W.-H. Zhang, *Inorg. Chem.*, 2018, **57**, 8382.
- 44 Q. Zou, X. Li, J. J. Zhang, J. Zhou, B. B. Sun and H. Tian, *Chem. Commun.*, 2012, **48**, 2095.
- 45 G.-Y. Lan, C.-C. Huang and H.-T. Chang, *Chem. Commun.*, 2010, **46**, 1257.
- 46 A. W. Zhu, Q. Qu, X. L. Shao, B. Kong and Y. Tian, *Angew. Chem., Int. Ed.*, 2012, **51**, 7185.
- 47 Y. H. Wang, C. Zhang, X. C. Chen, B. Yang, L. Yang, C. L. Jiang and Z. P. Zhang, *Nanoscale*, 2016, **8**, 5977.
- 48 (a) H. Kozłowski, M. Luczkowski, M. Remelli and D. Valensin, *Coord. Chem. Rev.*, 2012, **256**, 2129; (b) L. Li, M. Hou, L. Cao, Y. Xia, Z. Shen and Z. Hu, *Environ. Exp. Bot.*, 2018, **155**, 313; (c) J. Tan, S. He, S. Yan, Y. Li, H. Li, H. Zhang, L. Zhao and L. Li, *Protoplasma*, 2014, **251**, 1213; (d) Y. Liu, K. Ogawa and K. S. Schanze, *J. Photochem. Photobiol., C*, 2009, **10**, 173.
- 49 (a) Z. M. Hao, X. Z. Song, M. Zhu, X. Meng, S. N. Zhao, S. Q. Su, W. T. Yang, S. Y. Song and H. J. Zhang, *J. Mater. Chem. A*, 2013, **1**, 11043; (b) J. C. Sanchez, S. A. Urbas, S. J. Toal, A. G. DiPasquale, A. L. Rheingold and W. C. Trogler, *Macromolecules*, 2008, **41**, 1237; (c) B. Yan and Y.-F. Shao, *RSC Adv.*, 2014, **4**, 3318.
- 50 J.-L. Wang, Y.-R. Lu, H.-H. Li, J.-W. Liu and S.-H. Yu, *J. Am. Chem. Soc.*, 2017, **139**, 9921.
- 51 (a) A. B. Ganganboina, A. D. Chowdhury and R. Doong, *ACS Appl. Mater. Interfaces*, 2018, **10**, 614; (b) M. M. Zhang, M. L. Saha, M. Wang, Z. X. Zhou, B. Song, C. J. Lu, X. Z. Yan, X. P. Li, F. H. Huang, S. C. Yin and P. J. Stang, *J. Am. Chem. Soc.*, 2017, **139**, 5067; (c) S. M. Tawfik, J. Shim, D. Biechele-Speziale, M. Sharipov and Y. I. Lee, *Sens. Actuators, B*, 2018, **257**, 734.
- 52 M. Prudent and H. H. Girault, *Metallomics*, 2009, **1**, 157.
- 53 (a) L. Qin, L. X. Lin, Z. P. Fang, S. P. Yang, G. H. Qiu, J. X. Chen and W. H. Chen, *Chem. Commun.*, 2016, **52**, 132; (b) C. L. Tan, P. Yu, Y. L. Hu, J. Z. Chen, Y. Huang, Y. Q. Cai, Z. M. Luo, B. Li, Q. P. Lu, L. H. Wang, Z. Liu and H. Zhang, *J. Am. Chem. Soc.*, 2015, **137**, 10430.